An a posteriori time error indicator for adaptive flow solvers

Javad Sekhavati[a,b], Ramon Codina[a,b], Joan Baiges[a,b] and Ignacio Martínez-Suárez[a,b]

[a] *Universitat Politècnica de Catalunya, Jordi Girona 1-3, Edifici C1, 08034, Barcelona, Spain*

[b] *Centre Internacional de Mètodes Numèrics en Enginyeria (CIMNE), Edifici C1, Campus Nord UPC, Gran Capità S/N, 08034 Barcelona, Spain.*

javad.sekhavati@upc.edu (JS), ramon.codina@upc.edu (RC), joan.baiges@upc.edu (JB) and ignacio.martinez.suarez@upc.edu (IM)

Abstract

This study introduces a novel a posteriori time error indicator applied to a finite element flow solver. The proposed approach integrates stabilized finite element techniques in space and backward differentiation formula (BDF) schemes in time, adjusting time step sizes dynamically in unsteady flow simulations. The developed time error indicator and time adaptivity algorithm encompass monolithic and fractional step algorithms. In the case of fractional step algorithms, an additional term is incorporated in the error indicator to account for the error caused by the splitting. A series of numerical examples are presented to validate the reliability and robustness of the time error indicator across benchmark problems involving incompressible and isentropic compressible flows.

Keywords: BDF schemes; Time error indicator; Stabilized finite element methods; Fractional step schemes; Adaptivity; Variational multiscale method.

1. Introduction

The Navier-Stokes equations provide a fundamental framework for modeling a diverse range of applications, from aerodynamics and weather modeling to industrial processes and biomechanics. For compressible fluid flows, the isentropic formulation of these equations simplifies the thermodynamic behavior by assuming adiabatic processes without entropy change. Despite this simplification, the numerical solution of isentropic Navier-Stokes flow remains challenging because the continuity and momentum equations are nonlinearly coupled, adding significant complexity to the system. Developing efficient and accurate numerical schemes is therefore crucial for solving such systems [42]. In the context of numerical simulations, perhaps the most common approach is to discretize independently in space and time (i.e., using the method of lines). This is the approach we shall follow in this work, using finite elements for the space discretization and finite differences for the time approximation. The critical issue is to determine the appropriate mesh and time step sizes. In this respect, adaptive methods have emerged as indispensable tools, significantly advancing the field by balancing accuracy and computational cost [28]. A vital component of these methods are the error indicators, which aid in refining the mesh and time step size where necessary while maintaining coarser approximations in less sensitive areas. While a priori error estimates provide theoretical upper bounds on the error [24], a posteriori error indicators offer a more practical and efficient approach by evaluating the error after a numerical solution is obtained [9, 8]. These indicators play a crucial role in guiding adaptive schemes, particularly for problems

involving complex dynamics and evolving features, such as shock waves, vortices, and boundary layers in compressible flows [27, 14, 6, 12].

Most research on adaptive refinement algorithms for the Navier-Stokes equations has focused on spatial refinement, with comparatively less attention devoted to temporal refinement [26, 36, 6, 12]. However, several recent developments have introduced a posteriori time error indicators to support adaptive time stepping in unsteady flow simulations. Residual-based indicators, such as those introduced by [1], reconstruct a higher-order temporal approximation of the solution and evaluate its partial differential equation residual to derive rigorous upper bounds of the time discretization error. Reconstruction-based strategies, like the one proposed by [11], estimate the time error by evaluating the defect of a piecewise polynomial interpolant constructed from BDF2 solutions, enabling sharp and efficient temporal adaptivity. Gradient-based error indicators, as seen in [10, 25, 46], measure variations in the velocity gradient or divergence between successive time levels and offer simple, low-cost estimators suitable for time step size adaptivity. In this work, we will only consider adaptive refinement in time, and not in space.

These indicators are particularly valuable when coupled with variable time step integration methods, which allow the temporal resolution to adapt dynamically to the evolving behavior of the solution. In transient simulations, the time step size can significantly affect the overall accuracy of the solution. Among time integrators, backward differentiation formulas (BDFs) [48] are widely employed in computational fluid dynamics due to their stability in handling stiff systems [38, 30]. The implementation of adaptive time-stepping strategies is enabled by these methods, which must be guided by reliable a posteriori time error indicators. When properly combined, they significantly enhance both the accuracy and efficiency of unsteady flow simulations through dynamic adjustment of the time step size [28].

In this study, a time error indicator based on evaluating the difference between given and reconstructed higher order approximations of the time derivative, is applied to stabilized finite element flow solvers. The development of the time error indicator is done for the compressible isentropic Navier-Stokes equations, although it can be easily extended to the incompressible or fully compressible Navier-Stokes equations. The time error indicator includes a term for evaluating the splitting error introduced by classical projection or fractional step schemes used to enhance simulation runtime.

The proposed approach is developed in the context of the Variational Multi-Scale (VMS) method, a general variational framework for sub-grid scale (SGS) models [35]. The VMS approach is based on the separation of the unknown into a resolvable and a SGS part. An approximation for the SGS part is then sought, which allows to obtain a stable formulation in terms of the resolvable scales only [20]. Monolithically solving the VMS algebraic system of equations that arises after discretizing the continuous isentropic flow problem with the finite element method can be time-consuming and computationally expensive. In this case, fractional step or segregation methods (also called projection methods), which are based on the decomposition of differential operators either at the continuous level [16, 17, 44], or algebraic level, build computationally efficient systems that noticeably reduce the run time. However, the downside is that this introduces a new source of error to the system due to the splitting [3].

We propose first a time error indicator that expresses errors resulting from the time discretization using a monolithic algorithm. An additional term for the time error indicator in the context of fractional step schemes is then suggested to account for the new error source introduced by the segregation technique. The proposed method is validated through numerical experiments on benchmark problems involving incompressible and isentropic compressible flows. These results demonstrate that the time error indicator is reliable, and an adaptive algorithm based on it im-

proves the solution accuracy and enhances computational efficiency by reducing the number of time steps required to achieve a specified error tolerance. This flexible methodology is adaptable to a wide range of flow configurations and is a robust tool for diverse applications in academic research and industrial simulations.

The rest of the paper is organized as follows: Section 2 presents the governing equations alongside their variational formulation. Section 3 delivers the details of variable time step size BDF2 and BDF3 (second and third order backward differences) time integration schemes computed from a Taylor expansion. Section 4 presents the space approximation and derives the necessary modifications to the governing equations of monolithic and fractional step algorithms for accommodating variable-time stepping. Section 5 proposes a time error indicator, the additional error indicator term for fractional step algorithms, and a time adaptive algorithm. Followingly, Section 6 exemplifies the numerical experiments. Finally, Section 7 provides the conclusions.

2. Isentropic compressible flow formulation

2.1. The continuous problem

The isentropic Navier-Stokes equations for a Newtonian fluid in the computational domain $\Omega \subset \mathbb{R}^d$ (where $d = 2, 3$) and during a time interval $[0, t_\mathrm{f}]$ considering Newtonian isentropic conditions are:

$$\rho\partial_t \mathbf{u} + \rho(\mathbf{u}\cdot\nabla)\mathbf{u} - \mu\nabla^2\mathbf{u} - \frac{\mu}{3}\nabla(\nabla\cdot\mathbf{u}) + \nabla p = \mathbf{f} \qquad \text{in } \Omega, t \in (0, t_\mathrm{f}), \tag{1}$$

$$\partial_t \rho + (\mathbf{u}\cdot\nabla)\rho + \rho\nabla\cdot\boldsymbol{u} = 0 \qquad \text{in } \Omega, t \in (0, t_\mathrm{f}), \tag{2}$$

where ρ is the density, p is the pressure, $\mathbf{u}$ is the velocity field, and μ is dynamic viscosity which is assumed constant and $\mathbf{f}$ stand for the force vector. Initial and boundary conditions have to be appended to the differential equations (1)-(2).

Based on the principles of ideal gas behavior and simplified assumptions regarding isentropic flow, the equations that relate density and pressure in a compressible flow are (see Chapter 4 of [40] for details):

$$\frac{\rho_0}{\rho} = \left(1 + \frac{\gamma-1}{2}\mathrm{Ma}^2\right)^{\frac{1}{\gamma-1}}, \quad \frac{p_0}{p} = \left(1 + \frac{\gamma-1}{2}\mathrm{Ma}^2\right)^{\frac{\gamma}{\gamma-1}}, \tag{3}$$

where $()_0$ represents variables at the stagnation conditions, which describe the theoretical state that would result if the flow at any given point were isentropically brought to a complete stop, effectively eliminating any kinetic energy. γ is the adiabatic gas constant, Ma is the Mach number defined as $\mathrm{Ma} := |\mathbf{u}|/c_0$, where $|\mathbf{u}|$ is the modulus of the pointwise flow velocity, and c_0 is the speed of sound of an ideal gas, computed as $c_0 := \sqrt{\gamma R\Theta_0/M}$. Moreover, R [J/K-mol] is the universal gas constant. Θ_0 [K] and M [kg/mol] symbolize the temperature and the gas molar mass, respectively. From Eq. (3), one can readily get:

$$\frac{p_0}{p} = \left(\frac{\rho_0}{\rho}\right)^{\gamma}. \tag{4}$$

Upon differentiating both sides of Eq. (4) with respect to time and employing the ideal gas equation of state given by $p_0 M = \rho_0 R\Theta_0$, the following expression relating the time derivatives of pressure and density can be found:

$$\partial_t p = \frac{p_0}{\rho_0}\gamma\left(1 + \frac{\gamma-1}{2}\mathrm{Ma}^2\right)^{-1}\partial_t\rho$$

$$= \frac{R\Theta_0}{M}\gamma\left(1+\frac{\gamma-1}{2}\mathrm{Ma}^2\right)^{-1}\partial_t\rho. \tag{5}$$

Using the expression of the speed of sound

$$c = c_0\left(1+\frac{\gamma-1}{2}\mathrm{Ma}^2\right)^{-\frac{1}{2}}, \tag{6}$$

Eq. (5) can be written as

$$\partial_t p = c^2\partial_t\rho, \tag{7}$$

and, similarly,

$$\nabla p = c^2\nabla\rho. \tag{8}$$

Using Eqs. (7)-(8), the governing equations can be reformulated as

$$\rho\partial_t\mathbf{u} + \rho(\mathbf{u}\cdot\nabla)\mathbf{u} - \mu\nabla^2\mathbf{u} - \frac{\mu}{3}\nabla(\nabla\cdot\mathbf{u}) + \nabla p = \mathbf{f} \qquad \text{in } \Omega, t\in(0,t_\mathrm{f}), \tag{9}$$

$$\frac{1}{\rho c^2}\partial_t p + \frac{1}{\rho c^2}(\mathbf{u}\cdot\nabla)p + \nabla\cdot\mathbf{u} = 0 \qquad \text{in } \Omega, t\in(0,t_\mathrm{f}), \tag{10}$$

so that pressure derivatives substitute the density derivatives, and the solution of the isentropic compressible Navier-Stokes problem only depends on velocity and pressure. In these equations, the speed of sound c can be computed from Eq. (6).

2.2. Variational form

Let us define the space of square-integrable functions in the domain ω as $L^2(\omega)$, its norm by $\|\cdot\|_{L^2(\omega)}$ and denote the integral of the product of two generic functions in the region ω as $\langle\cdot,\cdot\rangle_\omega$. The subscript is omitted when $\omega=\Omega$. Let V^d and Q be defined as the functional spaces with appropriate regularity where velocities and pressure are well defined for each time $t\in(0,t_\mathrm{f})$. In these functional spaces with appropriate regularity, velocities, and pressure are well defined for each time $t\in(0,t_\mathrm{f})$. Note that V^d is a subspace of $H^1(\Omega)^d$ and Q of $L^2(\Omega)$; the additional regularity can be chosen in different ways to have a well defined problem (for example, bounded pressures would suffice). The variational form of the problem is: find $\mathbf{u}:(0,t_\mathrm{f})\to V^d$ and $p:(0,t_\mathrm{f})\to Q$ such that

$$B(\rho,\mathbf{u};[\mathbf{u},p],[\mathbf{v},q]) + B_\Gamma([\mathbf{u},p],\mathbf{v}) = \langle\mathbf{v},\mathbf{f}\rangle \tag{11}$$

for all test functions $\mathbf{v}\in V^d$ and $q\in Q$, where

$$\begin{aligned} B(\hat\rho,\hat{\mathbf{u}};[\mathbf{u},p],[\mathbf{v},q]) &= \langle\hat\rho\mathbf{v},\partial_t\mathbf{u}\rangle + \langle\hat\rho\mathbf{v},(\hat{\mathbf{u}}\cdot\nabla)\mathbf{u}\rangle + \mu\langle\nabla\mathbf{v},\nabla\mathbf{u}\rangle + \frac{\mu}{3}\langle\nabla\cdot\mathbf{v},\nabla\cdot\mathbf{u}\rangle \\ &\quad - \langle\nabla\cdot\mathbf{v},p\rangle + \left\langle\frac{1}{\hat\rho\hat c^2}q,\partial_t p\right\rangle + \left\langle\frac{1}{\rho\hat c^2}q,\mathbf{u}\cdot\nabla p\right\rangle + \langle q,\nabla\cdot\mathbf{u}\rangle, \\ B_\Gamma([\mathbf{u},p],\mathbf{v}) &= \langle\mathbf{v},\mathbf{n}\cdot\sigma(\mathbf{u},p)\rangle_\Gamma, \end{aligned} \tag{12}$$

$\hat{\mathbf{u}}$ represents the convective velocity, $\hat\rho$ a given density and $\hat c$ the speed of sound computed with it. Note that the tests functions have been placed in the first argument of the integrals. Given $\hat\rho$, $\hat{\mathbf{u}}$, $B(\hat\rho,\hat{\mathbf{u}};\cdot,\cdot)$ is a bilinear form. The stress tensor is defined as $\sigma(\mathbf{u},p) = -p\mathbf{I} + \mu\nabla\mathbf{u} + \frac{1}{3}\mu(\nabla\cdot\mathbf{u})\mathbf{I}$. Special consideration must be applied when imposing boundary conditions for the isentropic problem; further details are available in [41] and are summarized next.

2.3. Imposition of boundary conditions

The presented formulation aims to address flow and acoustic scales simultaneously, which leads to the necessity of appropriate boundary conditions for avoiding the refection of acoustic waves in the external boundaries. Several numerical methods have been developed to tackle this challenge (see, for instance, [29], [39], [31], and Chapter 4 of [23] for a detailed review). In this work we use two of these methodologies, depending on the considered numerical example at hand, the non-reflecting boundary condition (NRBC) and a Perfectly Matched Layer (PML). Since the description of these methodologies is quite extense, we include only a brief explanation here and we refer the reader to the corresponding references.

Non-reflecting boundary conditions (see [42]) are applied by decomposing the flow variables into time averaged quantites and oscillatory components around them. After this decomposition is introduced, a Nitsche type method is used to apply the conditions on the mean flow quantities, while a Sommerfeld type boundary condition is applied to the oscillatory component to eliminate the spurious reflections in the outer boundary. The PML approach we favor is based on a volume penalty term which forces the velocity and pressure to tend to zero in the regions close to the outer boundaries. The penalty term value changes in space so that in the region closer to the mechanical domain, the penalty term is small, and it becomes larger close to the outer domain (see [7, 42]).

3. BDF schemes with variable time step sizes

For the time discretization, we focus on backward difference schemes in the present work, although the proposed developments could also be applied to more complex time integration schemes. The BDF family is preferred due to its favorable stability properties. This section gathers the expressions for the BDF2 and BDF3 time integrators with variable time step sizes, which will be later employed for the adaptive time refinement algorithm.

We consider a partition $0 = t^0 < t^1 < \cdots < t^n < \cdots < t^N = t_\mathrm{f}$ of the time interval $[0, t_\mathrm{f}]$ and denote by $\delta t^n = t^{n+1} - t^n$ the time step size of the subinterval $[t^n, t^{n+1}]$. We also set $\delta t = \max_n\{\delta t^n\}$. It will be clear by the context whether the superscript of δt denotes time level (usually written as δt^n, $\delta t^{n+1}, \dots$) or power (e.g., δt^2, δt^3, δt^k).

3.1. BDF2 with variable time step size

The variable time step size BDF2 scheme can be derived from the second order Taylor expansion of a generic function $w(t)$ at the current time t^{n+1} evaluated at the two previous time steps, t^n and t^{n-1}. Denoting $w(t^n) \equiv w^n$ and using the notation $\frac{\mathrm{d}w}{\mathrm{d}t}\Big|^{n+1}$ to represent the time derivative of w evaluated at time t^{n+1}, we have that

$$
\begin{aligned}
w^n &= w^{n+1} - \left.\frac{\mathrm{d}w}{\mathrm{d}t}\right|^{n+1} \delta t^n + \frac{1}{2}\left.\frac{\mathrm{d}^2 w}{\mathrm{d}t^2}\right|^{n+1} (\delta t^n)^2 + O\left(\delta t^3\right), \\
w^{n-1} &= w^{n+1} - \left.\frac{\mathrm{d}w}{\mathrm{d}t}\right|^{n+1} (\delta t^n + \delta t^{n-1}) + \frac{1}{2}\left.\frac{\mathrm{d}^2 w}{\mathrm{d}t^2}\right|^{n+1} (\delta t^n + \delta t^{n-1})^2 + O\left(\delta t^3\right).
\end{aligned}
$$

From these expressions, the BDF2 approximation for the time derivative is found to be

$$
\left.\frac{\delta_2 w}{\delta t}\right|^{n+1} \equiv \alpha_1 w^{n+1} - \alpha_2 w^n + \alpha_3 w^{n-1} = \left.\frac{\mathrm{d}w}{\mathrm{d}t}\right|^{n+1} + O(\delta t^2), \tag{13}
$$

where $\frac{\delta_2}{\delta t}$ denotes the second-order backward differentiation operator used to approximate the time derivative at t^{n+1} and

$$\begin{aligned}\alpha_1 &= \frac{\delta t^{n-1} + 2\delta t^n}{\delta t^n(\delta t^{n-1} + \delta t^n)},\\ \alpha_2 &= (\alpha_1 + \alpha_3),\\ \alpha_3 &= \frac{\delta t^n}{\delta t^{n-1}(\delta t^{n-1} + \delta t^n)}.\end{aligned}$$

3.2. BDF3 with variable time step size

By the same approach, the formulation of the BDF3 scheme with variable time step size can be obtained from the Taylor expansions:

$$\begin{aligned}w^n &= w^{n+1} - \left.\frac{\mathrm{d}w}{\mathrm{d}t}\right|^{n+1} \delta t^n + \frac{1}{2}\left.\frac{\mathrm{d}^2w}{\mathrm{d}t^2}\right|^{n+1} (\delta t^n)^2 - \frac{1}{6}\left.\frac{\mathrm{d}^3w}{\mathrm{d}t^3}\right|^{n+1} (\delta t^n)^3 + O\left(\delta t^4\right),\\ w^{n-1} &= w^{n+1} - \left.\frac{\mathrm{d}w}{\mathrm{d}t}\right|^{n+1} (\delta t^n + \delta t^{n-1}) + \frac{1}{2}\left.\frac{\mathrm{d}^2w}{\mathrm{d}t^2}\right|^{n+1} (\delta t^n + \delta t^{n-1})^2\\ &\quad - \frac{1}{6}\left.\frac{\mathrm{d}^3w}{\mathrm{d}t^3}\right|^{n+1} (\delta t^n + \delta t^{n-1})^3 + O(\delta t^4),\\ w^{n-2} &= w^{n+1} - \left.\frac{\mathrm{d}w}{\mathrm{d}t}\right|^{n+1} (\delta t^n + \delta t^{n-1} + \delta t^{n-2})) + \frac{1}{2}\left.\frac{\mathrm{d}w}{\mathrm{d}t}\right|^{n+1} (\delta t^n + \delta t^{n-1} + \delta t^{n-2})^2\\ &\quad - \frac{1}{6}\left.\frac{\mathrm{d}^3w}{\mathrm{d}t^3}\right|^{n+1} (\delta t^n + \delta t^{n-1} + \delta t^{n-2})^3 + O(\delta t^4).\end{aligned}$$

Now, the BDF3 approximation to the time derivative that is obtained is:

$$\left.\frac{\delta_3 w}{\delta t}\right|^{n+1} \equiv \alpha_1 w^{n+1} - \alpha_2 w^n + \alpha_3 w^{n-1} + \alpha_4 w^{n-2} = \left.\frac{\mathrm{d}w}{\mathrm{d}t}\right|^{n+1} + O(\delta t^3), \tag{14}$$

where $\frac{\delta_3}{\delta t}$ denotes the third-order backward differentiation operator used to approximate the time derivative at t^{n+1}, with coefficients

$$\begin{aligned}\alpha_1 &= -(\alpha_2 + \alpha_3 + \alpha_4),\\ \alpha_2 &= \frac{(\delta t^n + \delta t^{n-1})(\delta t^n + \delta t^{n-1} + \delta t^{n-2})}{\delta t^n \delta t^{n-1}(\delta t^{n-1} + \delta t^{n-2})},\\ \alpha_3 &= \frac{\delta t^n(\delta t^n + \delta t^{n-1} + \delta t^{n-2})}{\delta t^{n-1}\delta t^{n-2}(\delta t^n + \delta t^{n-1})},\\ \alpha_4 &= -\frac{\delta t^n(\delta t^n + \delta t^{n-1})}{\delta t^{n-2}(\delta t^{n-1} + \delta t^{n-2})(\delta t^n + \delta t^{n-1} + \delta t^{n-2})}.\end{aligned}$$

4. Discretized problem

The detailed derivation of the finite element isentropic compressible Navier-Stokes equations and imposition of the boundary conditions is presented in [41]. In this section, the necessary modifications that these equations require to accommodate variable-time stepping are described.

4.1. Monolithic algebraic system with variable time step size

Let $\mathcal{T}_h = \{K\}$ represent a regular-shaped and conforming partition of the domain Ω, such that $\bar{\Omega} = \cup_{K\in\mathcal{T}_h} K$. This triangulation is characterized by the maximum mesh size, defined as $h := \max\{h_K | K \in \mathcal{T}_h\}\}$, where $h_K = \mathrm{diam}(K)$ is the diameter of each element $K \in \mathcal{T}_h$. Let us now define $V_h^d \subset V^d$ and $Q_h \subset Q$ as the finite element spaces for velocity and pressure, respectively, that correspond to the triangulation.

The final discrete formulation using the Galerkin approach is as follows: given $\mathbf{u}_h^{n-k+1}, \ldots, \mathbf{u}_h^n \in V_h^d$ and $p_h^{n-k+1}, \ldots, p_h^n \in Q_h$, find $\mathbf{u}_h^{n+1} \in V_h^d$ and $p_h^{n+1} \in Q_h$ such that

$$\left\langle \mathbf{v}_h, \rho^{n+1} \left.\frac{\delta_k \mathbf{u}_h}{\delta t}\right|^{n+1} \right\rangle + \langle \mathbf{v}_h, \rho^{n+1} (\mathbf{u}_h^{n+1} \cdot \nabla)\mathbf{u}_h^{n+1} \rangle + \mu \langle \nabla \mathbf{v}_h, \nabla \mathbf{u}_h^{n+1} \rangle + \frac{\mu}{3} \langle \nabla \cdot \mathbf{v}_h, \nabla \cdot \mathbf{u}_h^{n+1} \rangle - \langle \nabla \cdot \mathbf{v}_h, p_h^{n+1} \rangle = \langle \mathbf{v}, \mathbf{f}^{n+1} \rangle, \tag{15}$$

$$\left\langle q_h, \frac{1}{\rho^{n+1}(c^2)^{n+1}} \left.\frac{\delta_k p_h}{\delta t}\right|^{n+1} \right\rangle + \left\langle q_h, \frac{1}{\rho^{n+1}(c^2)^{n+1}} \mathbf{u}_h^{n+1} \cdot \nabla p_h^{n+1} \right\rangle + \langle q_h, \nabla \cdot \mathbf{u}_h^{n+1} \rangle = 0, \tag{16}$$

for all test functions $\mathbf{v}_h \in V_h^d$ and $q_h \in Q_h$. Of course, the k-th order BDF scheme ($k \geq 2$) has to be initialized for $n = 1, \ldots, k-1$ either with lower order schemes or with other finite difference approximations.

In the case of $\mathbf{P}^{n+1}$ representing the unknown nodal values of the pressure, and $\mathbf{U}^{n+1}$ representing the unknown nodal values of the velocity at each time step, the algebraic system structure of the variational formulation of the isentropic compressible Navier-Stokes equations manifests from Eqs. (15) and (16) in

$$\mathbf{M_u} \left.\frac{\delta_k \mathbf{U}}{\delta t}\right|^{n+1} + \mathbf{K_u}(\mathbf{U}^{n+1})\mathbf{U}^{n+1} + \mathbf{G}\mathbf{P}^{n+1} = \mathbf{F}^{n+1}, \tag{17}$$

$$\mathbf{M}_p \left.\frac{\delta_k \mathbf{P}}{\delta t}\right|^{n+1} + \mathbf{K}_p(\mathbf{U}^{n+1})\mathbf{P}^{n+1} + \mathbf{D}\mathbf{U}^{n+1} = \mathbf{0}, \tag{18}$$

where subscripts $()_\mathbf{u}$, $()_p$ refer to the momentum and continuity equation matrices.

4.2. Pressure-correction fractional step scheme with variable time step size

An essential part of the time error indicator to be proposed later is to estimate the segregation error in time of the fractional step scheme we shall use. The segregation technique approach employed here is a pressure correction scheme developed at the algebraic level [41]. It consists of three steps. In the first step, an intermediate velocity is computed based on previously known pressure and velocity values. The second step uses the intermediate velocity to compute the pressure, and the velocity is finally corrected in the third step. The resulting algebraic system is:

$$\mathbf{M_u} \left.\frac{\delta_k \tilde{\mathbf{U}}}{\delta t}\right|^{n+1} + \mathbf{K_u}(\tilde{\mathbf{U}}^{n+1})\tilde{\mathbf{U}}^{n+1} = \mathbf{F}^{n+1} - \mathbf{G}\hat{\mathbf{P}}_{k-1}^{n+1}, \tag{19}$$

$$\mathbf{M}_p \left.\frac{\delta_k \mathbf{P}}{\delta t}\right|^{n+1} + \mathbf{K}_p(\tilde{\mathbf{U}}^{n+1})\mathbf{P}^{n+1} - \frac{1}{\alpha_1}\mathbf{L}\mathbf{P}^{n+1} = -\mathbf{D}\tilde{\mathbf{U}}^{n+1} - \frac{1}{\alpha_1}\mathbf{L}\hat{\mathbf{P}}_{k-1}^{n+1}, \tag{20}$$

$$\alpha_1 \mathbf{M_u}\mathbf{U}^{n+1} = \alpha_1 \mathbf{M_u}\tilde{\mathbf{U}}^{n+1} - \mathbf{G}(\mathbf{P}^{n+1} - \hat{\mathbf{P}}_{k-1}^{n+1}), \tag{21}$$

where the matrices $\mathbf{K_u}$ and $\mathbf{K}_p$ represent the nonlinearity of the problems, which is dependent on the vector of unknown velocities. The variable $\tilde{\mathbf{U}}^{n+1}$ is the intermediate velocity, and variable $\hat{\mathbf{P}}_{k-1}^{n+1}$

is an auxiliary extrapolation of the pressure of order $k-1$. Note that $\mathbf{K_u}$ and $\mathbf{K}_p$ are evaluated with $\tilde{\mathbf{U}}^{n+1}$. Matrix $\mathbf{L}$ is a Laplacian matrix obtained using the gradient of standard shape functions. On top of the above formulations, the essential boundary conditions for isentropic formulations are properly adapted but not described here for brevity (see Section 2.3). In this regard, the reader is referred to Section 5.2 of [41] for a detailed discussion on implementation details and treatment of boundary terms.

4.3. Term-by-term stabilizations and final algebraic formulation

Up to this point, we have considered that the space discretization is based on the Galerkin finite element method. This requires appropriate inf-sup conditions to be satisfied for the velocity and pressure interpolations and may lead to numerical oscillations (and, very often, failure to converge) when the convective terms are important. The application of a proper stabilization technique is the final ingredient for a robust and consistent formulation. This technique enables the solution of highly convective problems, avoiding spurious solutions and instabilities, and, at the same time, allows the use of equal order interpolation for the velocity and the pressure without the need to fulfill the inf-sup condition [13, 2, 37]. The stabilized formulation used in this work is based on the Orthogonal Sub-Grid Scale concept within the VMS framework. For a detailed review, the reader is referred to [20], and for the final stabilized formulations and deriving procedure, to [41].

The terms to be added to the Galerkin ones are consistent, in the sense that when the mesh is refined they vanish at the appropriate rate, and are based on an approximation to the part of the solution which cannot be represented by the finite element mesh, the SGSs. The stabilized formulation is obtained by adding to Eq. (15)-(16) the terms:

$$
\begin{aligned}
&-\sum_{K\in\mathcal{T}_h}\langle\rho\mathbf{u}_h\cdot\nabla\mathbf{v}_h,\breve{\mathbf{u}}_1\rangle_K-\sum_{K\in\mathcal{T}_h}\langle\nabla\cdot\mathbf{v}_h,\breve{p}_1\rangle_K\\
&\quad-\sum_{K\in\mathcal{T}_h}\langle\nabla q_h,\breve{\mathbf{u}}_2\rangle_K-\sum_{K\in\mathcal{T}_h}\left\langle\frac{1}{c^2\rho}\mathbf{u}_h\cdot\nabla q_h,\breve{p}_2\right\rangle_K.
\end{aligned}
\tag{22}
$$

Here $\breve{\mathbf{u}}_1$ and $\breve{\mathbf{u}}_2$ are referred to as velocity SGSs and $\breve{p}_1$ and $\breve{p}_2$ as pressure SGSs. These stabilization terms are obtained by accounting for the SGSs contribution in the weak form of the problem. After further manipulations and some key approximations, the four SGSs $\breve{\mathbf{u}}_1$, $\breve{\mathbf{u}}_2$, $\breve{p}_1$ and $\breve{p}_2$ can be obtained from the following time dependent equations:

$$
\begin{aligned}
&\rho\partial_t\breve{\mathbf{u}}_1+\tau_1^{-1}\breve{\mathbf{u}}_1=-P_h^{\perp}\left[\rho\mathbf{u}_h\cdot\nabla\mathbf{u}_h\right], && \frac{1}{c^2\rho}\partial_t\breve{p}_1+\tau_2^{-1}\breve{p}_1=-P_h^{\perp}\left[\nabla\cdot\mathbf{u}_h\right],\\
&\rho\partial_t\breve{\mathbf{u}}_2+\tau_1^{-1}\breve{\mathbf{u}}_2=-P_h^{\perp}\left[\nabla p_h\right], && \frac{1}{c^2\rho}\partial_t\breve{p}_2+\tau_2^{-1}\breve{p}_2=-P_h^{\perp}\left[\frac{1}{c^2\rho}\mathbf{u}_h\cdot\nabla p_h\right],
\end{aligned}
$$

with zero initial condition for all of them, and where $P_h^{\perp}$ is the projection to the space orthogonal to the appropriate finite element space, either of velocities or of pressure. These equations can be integrated with the same BDF scheme as the equations for the finite element scales. Note that the SGSs need to be stored to integrate these equations in time.

The so-called stabilization parameters τ_1 and τ_2 are defined over each element $K\in\mathcal{T}_h$. They are an approximation to the inverse of the equation differential operators, which following a Fourier analysis can be defined as (see [18]):

$$
\tau_1=\left[c_1\frac{\mu}{h^2}+c_2\rho\frac{|\mathbf{u}_h|_K}{h}\right]^{-1},\qquad \tau_2=\frac{h^2}{c_1\tau_1},
\tag{23}
$$

where $|\mathbf{u}_h|_K$ is the mean Euclidean norm of the velocity in each element $K \in \mathcal{T}_h$. The algorithmic constants c_1 and c_2 can be set to (see [19]):

$$c_1 = \frac{4}{r^4}, \quad c_2 = \frac{2}{r},$$

where r is the order of the finite element interpolation.

The additional terms in Eq. (22) modify the weak forms of the momentum and continuity equations and need to be calculated at each time step to obtain a stabilized formulation. The final matrix system has the same algebraic structure as (17)-(18), with the addition of two stabilization matrices, $\mathbf{S_u}$ and $\mathbf{S}_p$, which originate from Eq. (22) evaluated with the intermediate velocity $\tilde{\mathbf{u}}_h$ in the case of fractional step schemes. The terms tested by $\mathbf{v}_h$ contribute to $\mathbf{S_u}$ and those tested by q_h contribute to $\mathbf{S}_p$.

Let us show now the equations of the resulting fractional step scheme, now considering the linearized form using a fixed-point method. Denoting with a second superscript the iteration counter, the intermediate velocity nodal values are the converged solution of the following problem: given $\tilde{\mathbf{U}}^{n+1,i}$ at iteration i, find $\tilde{\mathbf{U}}^{n+1,i+1}$ by solving

$$\mathbf{M_u} \left. \frac{\delta_k \tilde{\mathbf{U}}^{n+1,i+1}}{\delta t} \right|^{n+1} + \mathbf{K_u}(\tilde{\mathbf{U}}^{n+1,i})\tilde{\mathbf{U}}^{n+1,i+1} + \mathbf{S_u}(\tilde{\mathbf{U}}^{n+1,i})\tilde{\mathbf{U}}^{n+1,i+1} = \mathbf{F}^{n+1} - \mathbf{G}\hat{\mathbf{P}}_{k-1}^{n+1}, \tag{24}$$

which corresponds to the linearization and stabilization of Eq. (19). For the first iteration, the nonlinear terms are computed using $\tilde{\mathbf{U}}^{n+1,0} = \mathbf{U}^n$, and non-linear iterations are performed until the desired convergence tolerance is reached.

The pressure $\mathbf{P}^{n+1}$ is determined based on the intermediate velocity calculated from Eq. (24) as:

$$\mathbf{M}_p \left. \frac{\delta_k \mathbf{P}}{\delta t} \right|^{n+1} + \mathbf{K}_p(\tilde{\mathbf{U}}^{n+1})\mathbf{P}^{n+1} + \mathbf{S}_p(\tilde{\mathbf{U}}^{n+1})\mathbf{P}^{n+1} - \frac{1}{\alpha_1}\mathbf{L}\mathbf{P}^{n+1} = -\mathbf{D}\tilde{\mathbf{U}}^{n+1} + \frac{1}{\alpha_1}\mathbf{L}\widehat{\mathbf{P}}_{k-1}^{n+1}, \tag{25}$$

which is nothing but the stabilized form of Eq. (20). The additional stabilization term in the pressure ($\mathbf{S}_p(\tilde{\mathbf{U}}^{n+1})\mathbf{P}^{n+1}$) does not need to be linearized, as the intermediate velocity ($\tilde{\mathbf{U}}^{n+1}$) is already known when the pressure is computed.

When dealing with orthogonal projections ($P_h^{\perp}$) in Eqs. (24)-(25), the resulting matrices from the orthogonal projection of the unknowns display a wide stencil. In this scenario, the projection is computed using known values from either the previous iteration or time step (see [41] for details).

The equation for the end-of-step velocity $\mathbf{U}^{n+1}$ is still Eq. (21).

5. A posteriori error indicators

The time adaptivity algorithm, to be discussed later in detail, aims to adaptively adjust the time step size to ensure that the time discretization error meets the required tolerance, which is defined as a factor of the space discretization error. In this case, the existence of a space error indicator on top of the time error indicator will be crucial to adapt the time step size and to ensure an equilibrium between the spatial and temporal error sources.

5.1. A posteriori space error indicator

As said above, in addition to the proposed a posteriori time error indicator, an a posteriori space error indicator is necessary to relate the former to the latter and design the adaptive algorithm, which is also proposed. The goal is not to create a new a posteriori space error indicator. Instead, any existing options from the literature can be utilized. Specifically, an estimate based on the concept of SGSs is presented in [4, 21] (see also [32, 33, 34, 47]).

Even though it is not always appropriate for flows with significant convection, because of its simplicity we will use the Zienkiewicz-Zhu (ZZ) [49, 50] spatial error indicator for the velocity field for our numerical experiments, which is defined as:

$$\eta_x^n := \frac{\|P_h(\nabla \mathbf{u}_h^n) - \nabla \mathbf{u}_h^n\|_{L^2(\Omega)}}{\|P_h(\nabla \mathbf{u}_h^n)\|_{L^2(\Omega)}}, \quad n = 1, \ldots, N, \tag{26}$$

where P_h is the $L^2(\Omega)$-projection onto the finite element space. The rationale for this expression is that the projected velocity gradient is a better approximation of the exact one than the one computed directly from the discrete velocity. The a posteriori space error indicator is used only to assess the spatial component of the total error and to interpret its interaction with temporal errors.

5.2. A posteriori time error indicator

Suppose that we have computed the finite element sequence $\mathbf{u}_h^0, \mathbf{u}_h^1, \ldots, \mathbf{u}_h^n$ up to the time level $n \leq N$, and this has been obtained using a BDF scheme of order k, BDF-k, with its associate approximation to the time derivative at time t^n. The idea to design an a posteriori error indicator is that a better approximation to the time derivative could be obtained using the BDF scheme of order $k+1$, BDF-$(k+1)$, even if it is applied to the sequence obtained with BDF-k. Therefore, the time error indicator we propose for the velocity is:

$$\eta_{t,\mathrm{BDF}}^n = \frac{\left\| \left| \frac{\delta_{k+1}\mathbf{u}_h}{\delta t} \right|^n - \left| \frac{\delta_k \mathbf{u}_h}{\delta t} \right|^n \right\|_{L^2(\Omega)}}{\left\| \left| \frac{\delta_{k+1}\mathbf{u}_h}{\delta t} \right|^n \right\|_{L^2(\Omega)}}, \quad n = k+1, \ldots, N, \tag{27}$$

which is the difference between the BDF approximation of order $k = 1, 2, ...$ and that of one order higher $(k+1)$. Note that the heuristic motivation of (27) for the time error is similar to that of (26) for the space error. In the numerical section test cases we have used $k = 2$, i.e., the difference between BDF3 and BDF2 has been used as the time error indicator. At this point, let us highlight the difference between our proposal and two other error indicators that can be found in the literature. In [15] an expression like (27) is proposed, although the first term is not a reconstruction from the BDF2 solution, but indeed computed from the BDF3 scheme. In [11] the idea proposed is to reconstruct a quadratic polynomial in time from the velocity solution at three time levels, compute the time derivative of this reconstruction and then compute the L^2-norm in time of the difference between this reconstructed derivative and the one obtained from the BDF scheme, considered piecewise constant in a time interval.

Eq. (27) provides an estimate for the error due to the approximation of the time derivative. However, in the fractional step scheme we are using, there is also an error in time due to the splitting. We estimate this error by making it proportional to the difference between the intermediate velocity $\tilde{\mathbf{u}}_h^n$ and the end-of-step one, $\mathbf{u}_h^n$, that is to say,

$$\eta_{t,\mathrm{FS}}^n = \frac{\|\tilde{\mathbf{u}}_h^n - \mathbf{u}_h^n\|_{L^2(\Omega)}}{\|\mathbf{u}_h^n\|_{L^2(\Omega)}}. \tag{28}$$

Let us check in a formal (non rigorous) way that both (27) and (28) should be of order $O(\delta t^k)$. For the former, and considering that derivatives are bounded away from zero (this estimate is meaningless if the steady state is reached), we expect that

$$\left.\frac{\delta_k \mathbf{u}_h}{\delta t}\right|^n = \left.\frac{\partial \mathbf{u}_h}{\partial t}\right|_{t^n} + O(\delta t^k),$$

and therefore

$$\eta^n_{t,\mathrm{BDF}} = \frac{\left\| O(\delta t^{k+1}) + O(\delta t^k) \right\|_{L^2(\Omega)}}{\left\| \left.\frac{\partial \mathbf{u}_h}{\partial t}\right|_{t^n} + O(\delta t^{k+1}) \right\|_{L^2(\Omega)}} = O(\delta t^k).$$

For $\eta^n_{t,\mathrm{FS}}$ we just need to make use of Eq. (21), translating this equation into its discrete variational counterpart. Assuming that the pressure extrapolation has the expected order of approximation, this yields

$$\|\tilde{\mathbf{u}}^n_h - \mathbf{u}^n_h\|_{L^2(\Omega)} \sim \frac{1}{\alpha_1} \|\nabla p^n_h - \nabla \hat{p}^n_{h,k-1}\|_{L^2(\Omega)} \sim \delta t O(\delta t^{k-1}) = O(\delta t^k),$$

where $\sim$ stands for the order in δt.

The question now is how to combine (27) and (28). To do this, instead of normalizing $\eta^n_{t,\mathrm{FS}}$ by $\|\mathbf{u}^n_h\|_{L^2(\Omega)}$ we can normalize it by $\kappa^{-1} \left\| \left.\frac{\delta_{k+1}\mathbf{u}_h}{\delta t}\right|^n \right\|_{L^2(\Omega)}$ (recall that we assume time derivatives bounded away from zero), where κ is a user-defined parameter with units of time^{-1}. Accordingly, the total time discretization error indicator in fractional step schemes that we propose is:

$$\eta^n_t = \eta^n_{t,\mathrm{BDF}} + \eta^n_{t,\mathrm{FS}} = \frac{\left\| \left.\frac{\delta_{k+1}\mathbf{u}_h}{\delta t}\right|^n - \left.\frac{\delta_k \mathbf{u}_h}{\delta t}\right|^n \right\|_{L^2(\Omega)} + \kappa \left\| \tilde{\mathbf{u}}^n_h - \mathbf{u}^n_h \right\|_{L^2(\Omega)}}{\left\| \left.\frac{\delta_{k+1}\mathbf{u}_h}{\delta t}\right|^n \right\|_{L^2(\Omega)}}, \quad n = k+1, \ldots, N. \tag{29}$$

This error indicator is designed from heuristic arguments, but in the numerical examples we will show that it is a good approximation to the true error in time of the numerical formulation we use. The value of κ, which balances errors due to the discretization of the time derivative and the splitting errors, is also indicated in the numerical examples.

It should be noted that any other higher-order time integration methods, such as those from the Runge–Kutta family or time-discontinuous Galerkin (DG) methods, could also be used to achieve $(k+1)$-order accuracy. In this work we focus in the Backward Differentiation Formula (BDF) scheme of order $k+1$ due to its favorable properties for unsteady flow problems. BDF schemes are implicit and well-suited for stiff systems, offering stable long-time integration, efficient memory usage and have a low computational overhead when using higher-order approximations.

The error indicator given by (27) only estimates the error in the velocity time derivative. In the case of isentropic flows, we could also account for the error in the pressure time derivative. The natural way to combine both is determined by the rate of energy estimate that is obtained by taking $\mathbf{v} = \partial_t \mathbf{u}$ and $q = \partial_t p$ in (12). Among the different terms obtained by doing this, velocity and pressure time derivatives are combined as

$$\|\sqrt{\rho}\partial_t \mathbf{u}\|^2_{L^2(\Omega)} + \left\| \frac{1}{\sqrt{\rho}c} \partial_t p \right\|^2_{L^2(\Omega)},$$

and therefore the error indicator that we propose in this case is

$$\eta^n_{t,\mathrm{BDF}} = \frac{\left\| \sqrt{\rho^n} \left(\left| \frac{\delta_{k+1}\mathbf{u}_h}{\delta t} \right|^n - \left| \frac{\delta_k \mathbf{u}_h}{\delta t} \right| \right)^n \right\|_{L^2(\Omega)} + \left\| \frac{1}{\sqrt{\rho^n} c^n} \left(\left| \frac{\delta_{k+1} p_h}{\delta t} \right|^n - \left| \frac{\delta_k p_h}{\delta t} \right| \right)^n \right\|_{L^2(\Omega)}}{\left\| \sqrt{\rho^n} \left| \frac{\delta_{k+1}\mathbf{u}_h}{\delta t} \right|^n \right\|_{L^2(\Omega)} + \left\| \frac{1}{\sqrt{\rho^n} c^n} \left| \frac{\delta_{k+1} p_h}{\delta t} \right|^n \right\|_{L^2(\Omega)}}, \tag{30}$$

instead of (27). However, in the problems considered c is large and the errors in the pressure time derivative small, so that we have observed that (27) and (30) yield very similar results. We shall demonstrate this in one of the numerical examples.

5.3. Time adaptive algorithm

Eq. (29) implicitly provides a time error indicator as a function of the time step size of the current time level, δt^{n-1}, that is to say, we have $\eta^n_t = \eta^n_t(\delta t^{n-1})$ (recall that $\delta t^{n-1} = t^n - t^{n-1}$). Suppose that we wish to obtain the time step size δt^n to be used to obtain the solution at the time level $n+1$ so that it does not exceed a threshold error $\eta_{t,\max}$, i.e.,

$$\eta^{n+1}_t \leq \eta^{n+1}_{t,\max}. \tag{31}$$

The threshold $\eta^{n+1}_{t,\max}$ can be fixed by the user or related to the space error indicator to try to balance space and time errors, that is to say, we may set

$$\eta^{n+1}_{t,\max} = g\eta^{n+1}_x. \tag{32}$$

The factor g can be fixed to a value a priori or considered variable alongside the simulation depending on parameters such as Courant-Friedrichs-Lewy number (CFL) number, iteration errors, and solver residual norm. As it is explained in [22], this CFL number can be computed as $\frac{\delta t}{\tau_1}$ for each time step and within each element domain, where τ_1 is the stabilization parameter given by (23). We shall use Eq. (32) in our numerical examples.

The natural way to proceed is to solve *approximately* the nonlinear equation

$$\eta^{n+1}_t(\delta t^n) = \eta^{n+1}_{t,\max}, \tag{33}$$

and check that inequality (31) holds, or otherwise decrease δt^n.

Several alternatives can be used to approximate the solution of Eq. (33). Apart from the simple (but slow) bisection algorithm, one can use simplifications of Newton-Raphson's algorithm. Using a second superscript for the iteration counter, from a guess $\delta t^{n,i}$ we could compute $\delta t^{n,i+1}$ from:

$$\eta^{n+1,i+1}_t \approx \eta^{n+1,i}_t + \frac{\mathrm{d}\eta^{n+1}_t}{\mathrm{d}\delta t^n}(\delta t^{n,i+1} - \delta t^{n,i}) = \eta^{n+1}_{t,\max}.$$

This still requires an approximation to the derivative of η^{n+1}_t with respect to δt^n. A possibility would be

$$\frac{\mathrm{d}\eta^{n+1}_t}{\mathrm{d}\delta t^n} \approx \frac{\eta^n_t - \eta^{n-1}_t}{\delta t^{n-1} - \delta t^{n-2}}.$$

Another option, which is the one we have implemented, is to obtain the analytical expression of this derivative from Eq. (29), which is feasible if the dependency of the unknown $\mathbf{u}^{n+1}_h$ on δt^n is neglected. In any case, what is important is to check that condition (31) holds.

Finally, we have observed in practice that abrupt changes in the time step may deteriorate the nonlinear convergence performance of the final scheme. This is why we have introduced an "extreme clipping strategy", redefining

$$\delta t^n \leftarrow \max\{\delta t^n, f_{\min}\delta t^{n-1}\},$$
$$\delta t^n \leftarrow \min\{\delta t^n, f_{\max}\delta t^{n-1}\},$$

where $f_{\min} < 1$, $f_{\max} > 1$ are user-defined factors. This approach helps avoid significant fluctuations in time step sizes, mitigating the risk of instability and misinterpretation of results. The tolerances for the upper and lower bounds can be defined based on how strictly the time step sizes are to be clipped.

With all the ingredients described, the time adaptive algorithm we propose is summarized in Algorithm 1.

Algorithm 1: Time adaptive algorithm

Initialize the time step counter, $n = 1$;
for $n \leq N$ **do**
  compute the solution for the current specification of the mesh and time step size;
  for *all numerical integration points of every element in the domain* **do**
    if (algebraic system == Monolithic) **then**;
      Set $\eta_t^n \leftarrow \eta_{t,\text{BDF}}^n$ using Eq. (27);
    else if (algebraic system == fractional Step) **then**;
      Set $\eta_t^n \leftarrow \eta_{t,\text{BDF}}^n + \eta_{t,\text{FS}}^n$ using Eq. (29);
    end if
  end
  for *all numerical integration points of every element in the domain* **do**
    Add the contribution to η_x^n in Eq. (26) (for example);
  end
  set $\eta_{t,\max}^{n+1} = g\eta_x^{n+1}$ (g user-defined);
  compute δt^n by solving approximately Eq. (33);
  while *condition* (31) *is false* **do**
    $\delta t^n \leftarrow f\delta t^n$, with $f < 1$ (user-defined);
    Check (31) ;
  end
  set $\delta t^n \leftarrow \max\{\delta t^n, f_{\min}\delta t^{n-1}\}$;
  set $\delta t^n \leftarrow \min\{\delta t^n, f_{\max}\delta t^{n-1}\}$;
  set $n \leftarrow n + 1$;
end

6. Numerical Results

In this section, numerical examples are provided to illustrate the performance of the proposed method. The first case consists of a manufactured solution test, which helps to analyze the time discretization errors of the BDF2 and BDF3 schemes with variable time steps compared to the BDF2 and BDF3 schemes with constant time step sizes, respectively. Afterward, two other manufactured solutions are utilized to evaluate the performance of the proposed time error indicator

for the monolithic algorithm and, additionally, the correction term for the fractional step method compared to the actual error for different time step sizes. Except in one of the examples, (27) is used to compute the error due to the BDF time integration scheme. Furthermore, the performance of the time error indicator is examined in three practical cases: a flow over a cylinder for a low Reynolds incompressible viscous fluid, a 2D low-speed viscous flow over a cylinder at Ma = 0.0583, and a flow around a 3D NACA 0012 airfoil at Ma = 0.4.

The SI unit system is assumed in what follows. For the numerical cases of isentropic flows, the fluid is considered an ideal gas, with adiabatic coefficient $\gamma = 1.4$, molar mass M = 0.02897, and temperature $\Theta_0 = 293.15$. The speed of sound is $c_0 = 343.29$.

To avoid reflections from boundaries of the acoustic components of the solution, a numerical technique is required. For the aeolian tones example, boundary conditions are imposed using the strategy described in [41]. Mean flow Dirichlet boundary conditions are prescribed using Nitsche's method and a Sommerfeld-type non-reflecting boundary condition (NRBC) is used for the acoustic components of velocity and pressure. The parameter β of Nitsche's method is computed as $\beta = \beta_0(\frac{\mu}{h} + \rho\,|\mathbf{u}_h|)$ for a constant β_0 and mesh size h, which will be specified later.

For the example of the flow radiated by a NACA 0012 airfoil, the strategy used to avoid reflections from boundaries is a Perfectly Matched Layer (PML), detailed in [42, 43]. Note that this approach damps out all components of the solution in the region close to the boundary where the PML is applied, not only the acoustic components.

A value of 0.1 was selected for the Eq. (32) to ensure tighter control over the temporal error compared to the spatial error. When using fractional step schemes, the parameter κ appearing in Eq. (29) is calculated as $\kappa = \frac{\mu}{\rho l^2} + \frac{|\mathbf{u}_0|}{l}$ where l is a characteristic length of the problem and $|\mathbf{u}_0|$ the modulus of a characteristic velocity. The latter is taken as the far field velocity, whereas the former is the diameter of the cylinder for the two examples of flow over a cylinder and the chord length of the NACA 0012 profile for the flow over this airfoil.

The problem's nonlinearities are addressed using Picard's scheme, which results in a continuously decreasing relative error during successive iterations. A maximum of 20 iterations is allowed, which in all cases results in a relative convergence error of 10^{-6} in the L^2 norm. To solve the linear systems arising in each iteration, we have used the Biconjugate Gradients solver, BiCGstab [45], which is implemented in the PETSc parallel solver library [5] that we have used.

6.1. Manufactured solution tests

The manufactured solutions will be employed in what follows to numerically analyze the performance of the time integration schemes with variable time step sizes, in this case BDF2 and BDF3, against their version with constant time step size, and also the time error indicator's performance comparing it with the exact error for both monolithic and fractional step schemes. In all cases, the exact analytical solutions predefined are substituted into the governing equations to obtain the associated forcing terms.

The computational domain we consider is the unit square $\Omega = (0,1) \times (0,1) \subset \mathbb{R}^2$, with the velocity prescribed on the boundaries of Ω. The viscosity is set to $\mu = 0.1$ and the density to $\rho = 1$. A structured uniform mesh of bilinear quadrilateral elements of size $h = 0.015$ is used to discretize Ω for all manufactured solutions.

We will consider three manufactured solution pairs $[\mathbf{u}_i(x,y,t), p_i(x,y,t)]$, $i = 1,2,3$, where (x,y) are the Cartesian coordinates. These are given by

$$\mathbf{u}_1(x,y,t) = (\exp(-t)+1)\cos(\pi t)100[q(x)q'(y), -q'(x)q(y)], \quad q(z) = z^2(1-z)^2$$
$$p_1(x,y,t) = 100x^2$$

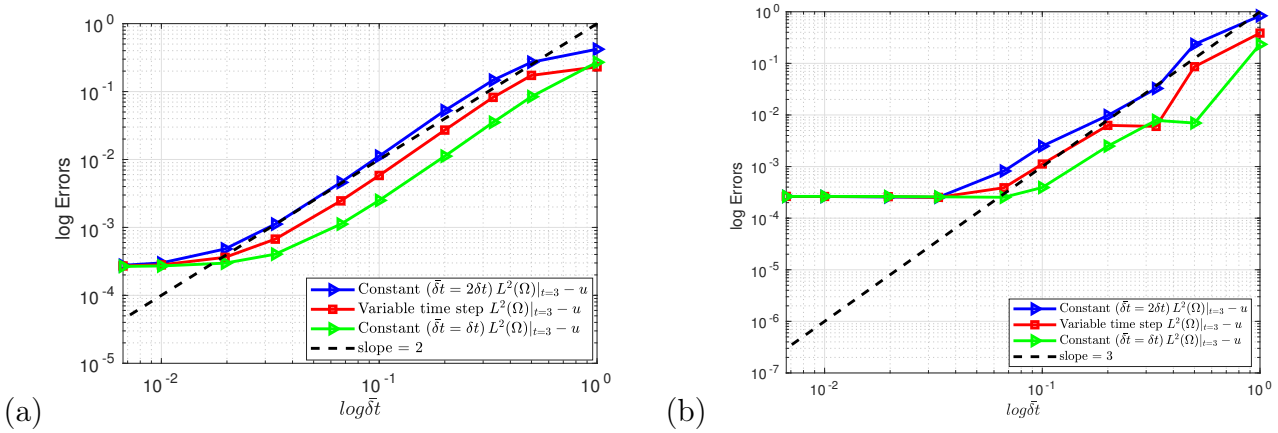

(a) (b)

Figure 1: Convergence tests results of normalized $L^2(\Omega)|_{t=3}$ velocity errors against the representative time step size ($\bar{\delta t}$) for the monolithic scheme and incompressible flows: (a) BDF2 scheme (b) BDF3 scheme.

$$
\begin{aligned}
\mathbf{u}_2(x,y,t) &= \mathbf{u}_1(x,y,t) \\
p_2(x,y,t) &= \pi\cos(\pi t)100(x-1)^2 \\
\mathbf{u}_3(x,y,t) &= (\sin(2t))[-\cos(x)\sin(y), \sin(x)\cos(y)], \\
p_3(x,y,t) &= -\frac{1}{4}(\sin^2(2t))[\cos(2x)+\cos(2y)].
\end{aligned}
$$

The first solution will be used to check the performance of the time integration schemes with variable time step size in terms of order of the error, and the other two for the analysis of the a posteriori time error indicator.

Fig. 1 presents the results of the convergence test using $[\mathbf{u}_1, p_1]$. The L^2-norm in space of the velocity error at time $t = 3$ is shown. First, a time step size convergence with a constant step size was performed using the BDF2 scheme (the green line in Fig. 1(a)). Secondly, the same computations were repeated, the only difference being that the time step sizes were multiplied by a factor of 2 (the blue line in Fig. 1(a)). Finally, the same convergence test was conducted using a variable step size BDF2 scheme, where the time step size was multiplied by two and divided by two every other time step, thus oscillating between the time step sizes of the previous two tests (the red line in Fig. 1(a)). The same procedure was repeated for the BDF3 scheme and shown in Fig.1(b). In both cases, the variable stepping recovers an error between those of the two constant time stepping cases, as expected, thus validating the behavior of the variable time step schemes. In order to permit the comparison of errors with the same axes of abcissae, these errors are plotted against $\bar{\delta t}$, with $\bar{\delta t} = \delta t$ for the green lines, $\bar{\delta t} = \delta t/2$ for the blue lines and, in the case of variable time step simulations, $\bar{\delta t}$ corresponds to the size of the odd time steps, while the even time steps are twice the size of the odd ones. Thus, $\bar{\delta t}$ is the same for all cases. In these and the forthcoming figures, the error saturates when the time step size tends to zero; this is because at a certain point the spatial errors dominate and the time discretization errors become relatively negligible.

The proposed time error indicator has been tested with manufactured solutions $[\mathbf{u}_2, p_2]$ and $[\mathbf{u}_3, p_3]$ for both monolithic and fractional-step algorithms, and also for both incompressible and isentropic flow regimes. In all cases, the BDF2 scheme has been used to discretize the temporal derivatives. Also, the errors of the solution variables have been measured in the discrete-in-time version of the space-time L^2 norms, and $L^2(\Omega)$ refers to the standard L^2-norm over the spatial domain Ω, while l^2 denotes the discrete L^2-norm over time steps. Therefore, the combined $l^2(L^2(\Omega))$ norm represents the global error accumulated in both space and time. Thus, for a generic function

of time and space w, if w^n is this function evaluated at time t^n we have that

$$\|w\|^2_{l^2(L^2(\Omega))} = \sum_{n=1}^{N} \|w^n\|^2_{L^2(\Omega)} \delta t^{n-1}.$$

Fig. 2 and Fig.3 show the convergence plots in the case of monolithic schemes, for incompressible and isentropic flows, respectively. The plots on the left show the error predicted by our a posteriori error indicator in (27) (for $k = 2$) and the true error. It is observed that the prediction is very good, and that the predicted error is a little higher than the true error. The plots on the right display the convergence curves for $\mathbf{u}$ and p, only for a reference. In this and the following figures it is observed that the rate of convergence is two for the velocity and at least one for the pressure, as expected.

δt	0.12	0.08	0.04	0.012	0.008	0.006	0.0048
$l^2(L^2(\Omega))$ – BDF EI	1.40E-02	8.58E-03	2.21E-03	1.94E-04	8.59E-05	4.82E-05	3.08E-05
$l^2(L^2(\Omega))$ – True Error	1.53E-02	8.45E-03	2.17E-03	1.93E-04	8.55E-05	4.81E-05	3.07E-05

Table 1: Convergence test results for the **monolithic** algorithm and **incompressible** flows using $[\mathbf{u}_3, p_3]$ (results corresponding to Fig. 2(c))

δt	0.12	0.08	0.04	0.012	0.008	0.006	0.0048	0.004
$l^2(L^2(\Omega))$ – BDF EI	5.62E-02	2.16E-02	5.11E-03	4.51E-04	1.99E-04	1.12E-04	7.17E-05	4.97E-05
$l^2(L^2(\Omega))$ – True Error	4.58E-02	1.43E-02	3.51E-03	5.01E-04	3.56E-04	3.12E-04	2.92E-04	2.82E-04

Table 2: Convergence test results for the **monolithic** algorithm and **isentropic** flows using $[\mathbf{u}_3, p_3]$ (results corresponding to Fig. 3(c))

δt	0.12	0.08	0.04	0.012	0.008	0.006	0.0048	0.004	0.003	0.0012	0.001	0.0008
$l^2(L^2(\Omega))$ – BDF + FS EI	1.101	0.533	0.144	1.32E-02	5.95E-03	3.35E-03	2.14E-03	1.49E-03	8.39E-04	1.34E-04	9.34E-05	5.98E-05
$l^2(L^2(\Omega))$ – True Error	1.950	0.654	0.146	1.34E-02	5.98E-03	3.38E-03	2.18E-03	1.54E-03	8.98E-04	2.94E-04	2.73E-04	2.58E-04

Table 3: Convergence test results for the **fractional step** algorithm and **isentropic** flows using $[\mathbf{u}_2, p_2]$ (results corresponding to Fig. 5(a))

To quantify the performance of the a posteriori error indicator, the numerical values that lead to Fig. 2(c), Fig. 3(c), and Fig. 5(a) have been reported in Table 1, Table 2, and Table 3 respectively.

Subsequently, Fig. 4 and Fig. 5 present the convergence plots in the case in which the fractional step scheme is employed, for incompressible and isentropic flows, respectively. Now, the plots on the left show the error predicted by our a posteriori error indicator in (29) (again for $k = 2$) and the true error. If the splitting error is not considered, the prediction (displayed in red) is poor, but when the estimate of the splitting error is introduced, the new prediction (displayed in dark blue) is very satisfactory. Nevertheless, let us point out that in our findings there was no universal coefficient κ for the splitting error term to ensure that the time error indicator is an upper bound of the true error.

The final test of this example is to check the influence of including the error in the pressure time derivative, i.e., the difference between using (27) and (30). Results are shown in Fig. 6. This figure displays the convergence with the time step size of the error estimator for the velocity alone

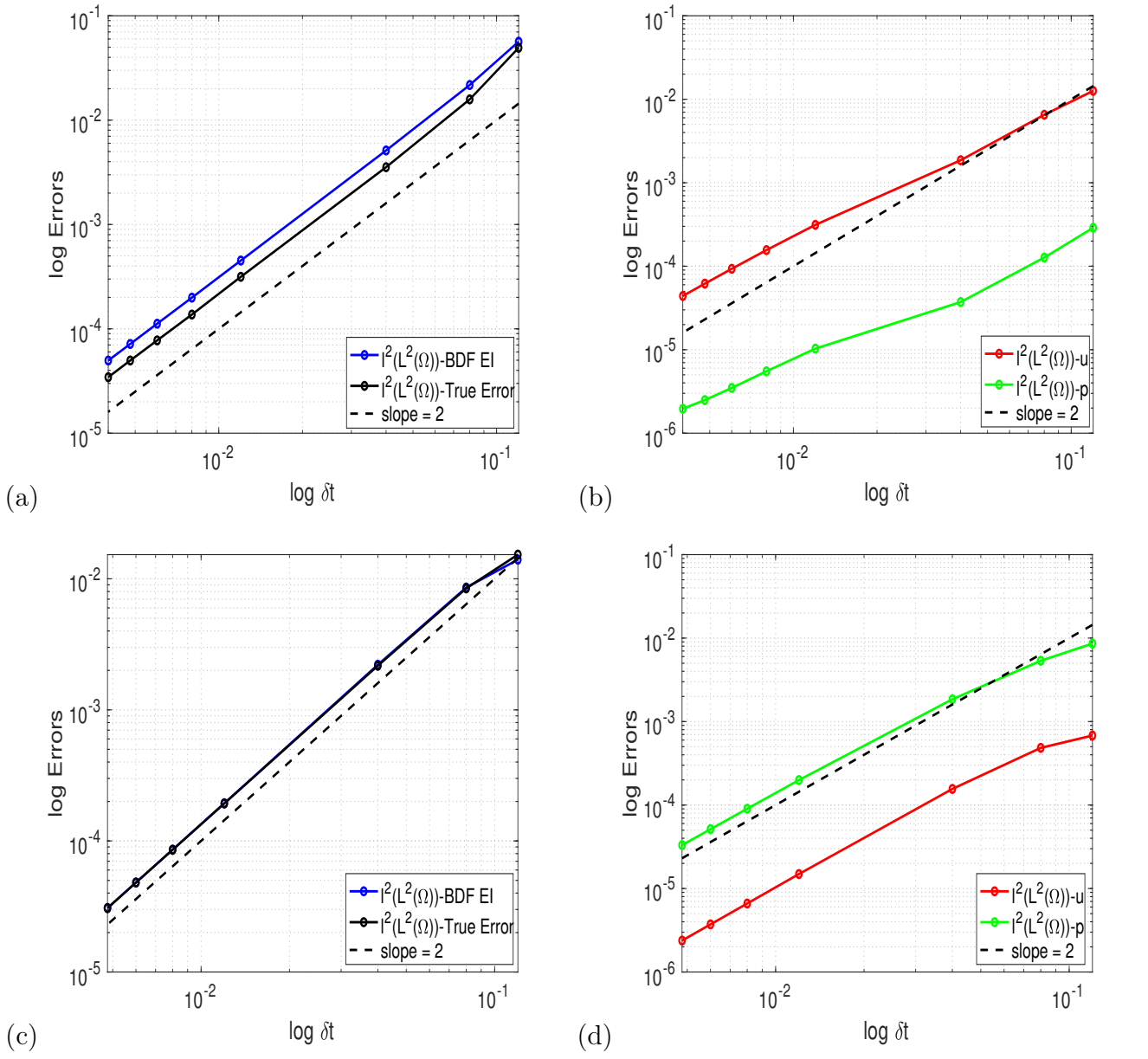

Figure 2: Convergence test results for the **monolithic** algorithm and **incompressible** flows. Top ((a) and (b)): solution $[\mathbf{u}_2, p_2]$; bottom ((c) and (d)): solution $[\mathbf{u}_3, p_3]$. Left ((a) and (c)): Comparison of the true error in $\partial_t \mathbf{u}$ and the predicted error; right: true error in $\mathbf{u}$ and p.

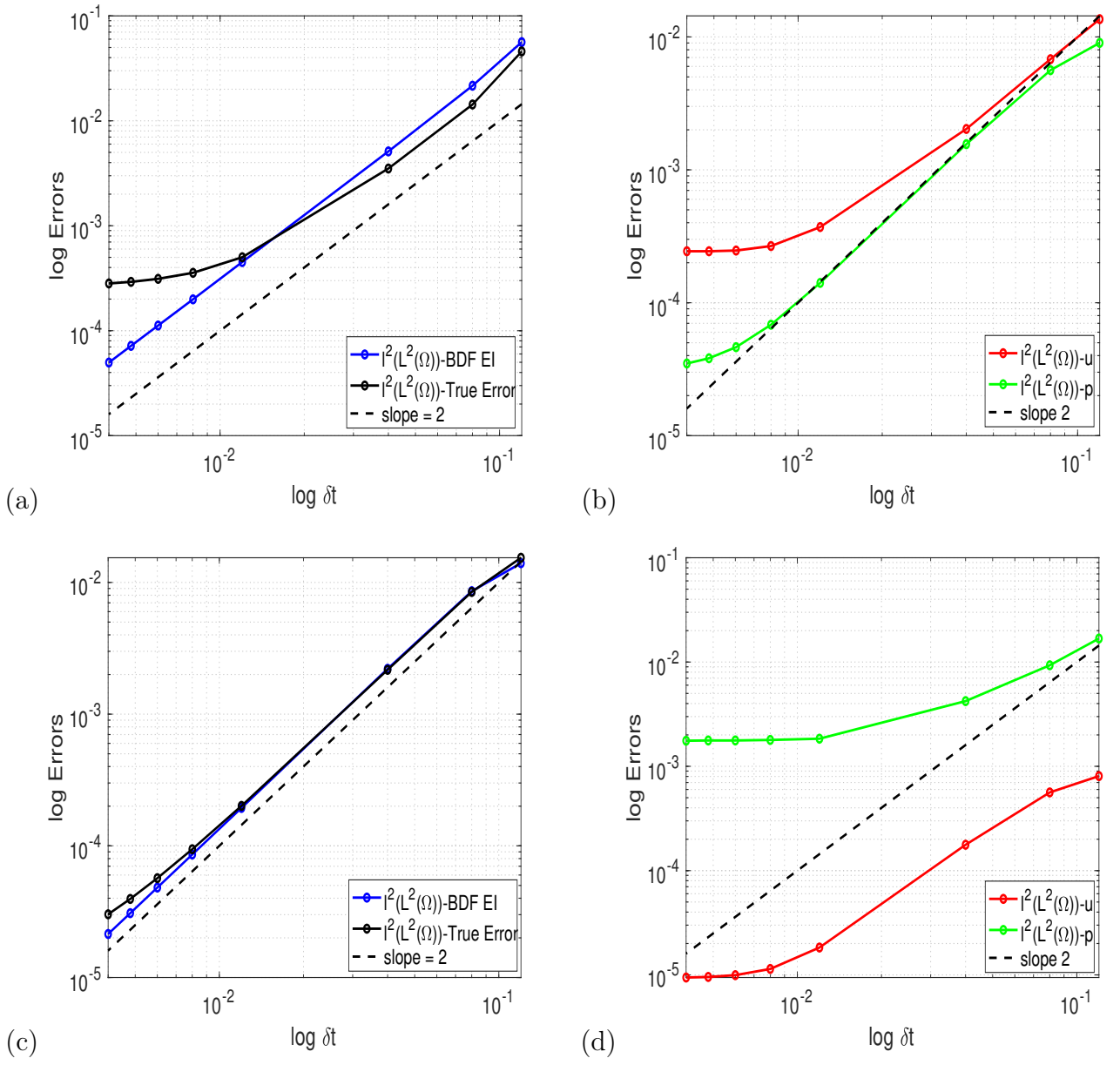

Figure 3: Convergence test results for the **monolithic** algorithm and **isentropic** flows. Top ((a) and (b)): solution $[\mathbf{u}_2, p_2]$; bottom ((c) and (d)): solution $[\mathbf{u}_3, p_3]$. Left ((a) and (c)): Comparison of the true error in $\partial_t \mathbf{u}$ and the predicted error; right: true error in $\mathbf{u}$ and p.

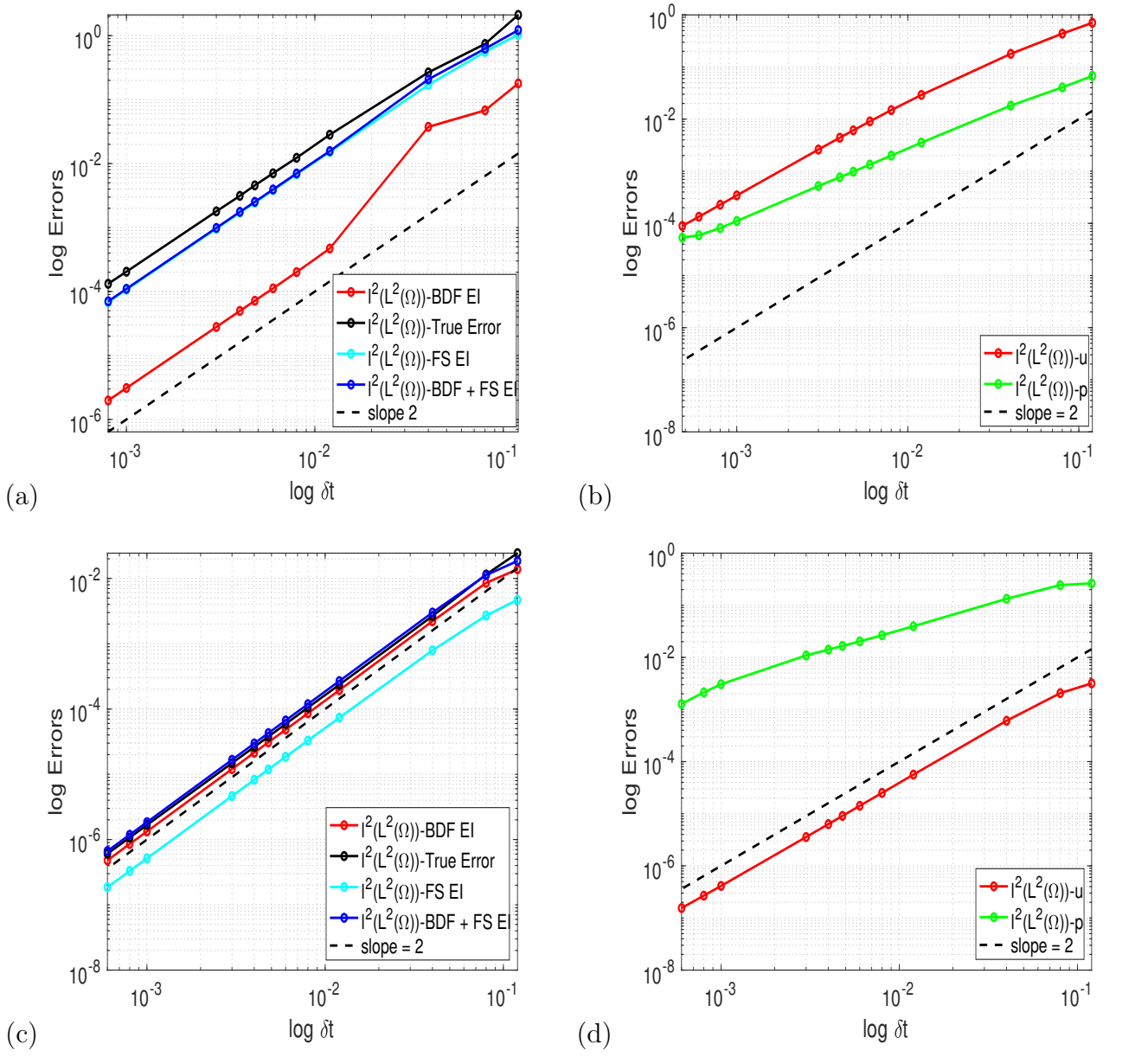

Figure 4: Convergence test results for the **fractional step** algorithm and **incompressible** flows. Top ((a) and (b)): solution $[\mathbf{u}_2, p_2]$; bottom ((c) and (d)): solution $[\mathbf{u}_3, p_3]$. Left ((a) and (c)): Comparison of the true error in $\partial_t \mathbf{u}$ and the predicted error; right: true error in $\mathbf{u}$ and p.

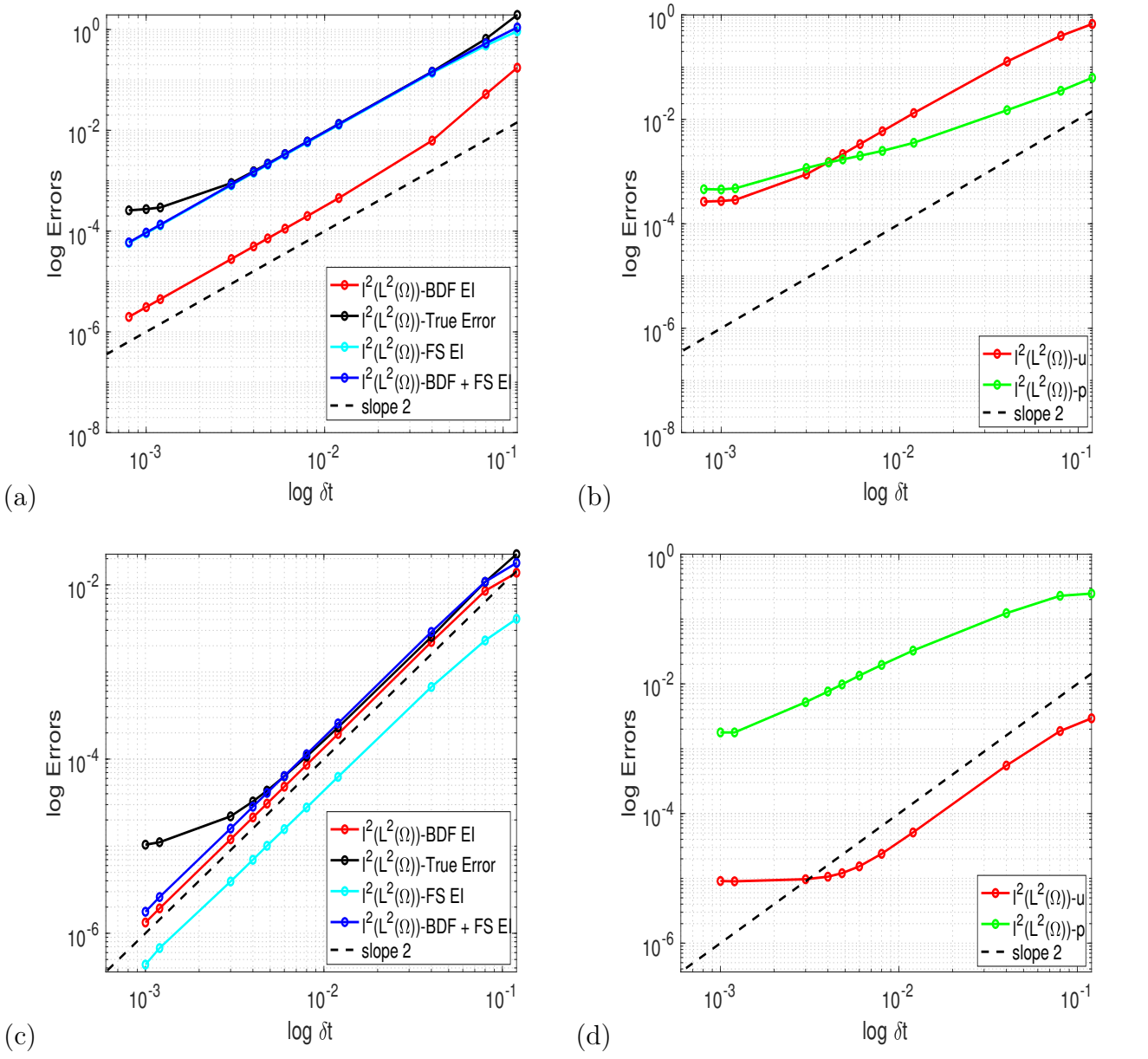

Figure 5: Convergence test results for the **fractional step** algorithm and **isentropic** flows. Top ((a) and (b)): solution $[\mathbf{u}_2, p_2]$; bottom ((c) and (d)): solution $[\mathbf{u}_3, p_3]$. Left ((a) and (c)): Comparison of the true error in $\partial_t \mathbf{u}$ and the predicted error; right: true error in $\mathbf{u}$ and p.

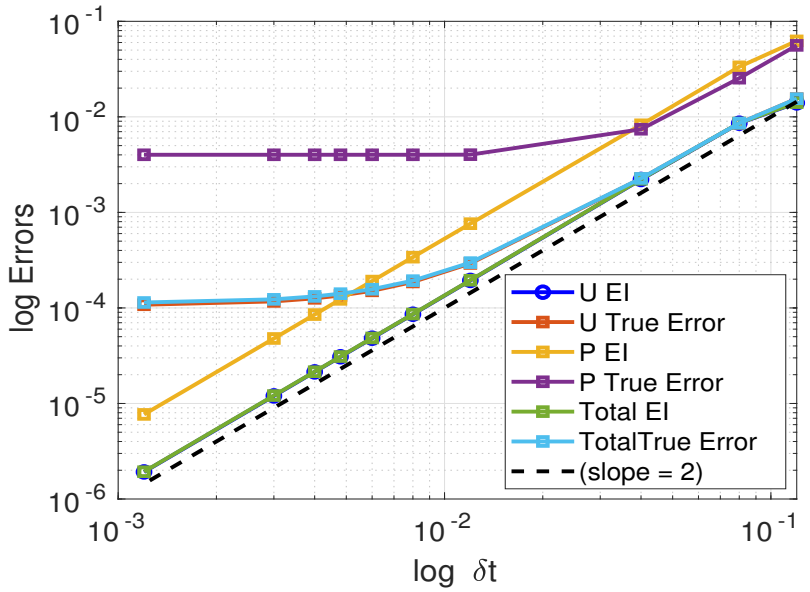

Figure 6: Comparison of the error evolution with and without the error in the pressure time derivative

.

(U EI), for the pressure (P EI) and for their combination given by (30) (Total EI), as well as the exact errors, denoted as "True Error" in Fig. 6. Because of the large value of c, it is seen that "U EI" and "Total EI" almost coincide, and this also happens for "U True Error" an "Total True Error". Thus, in what follows we will restrict ourselves to option (27).

6.2. Flow over a cylinder for a low Reynolds incompressible viscous flow

The problem domain of the second numerical example is a 2D rectangular area with a length of 16 units and a height of 8 units. A cylinder with a diameter of 1 unit is located at point (4, 4). The boundary conditions are as follows: a constant horizontal velocity $\mathbf{u} = (1, 0)$ is injected from the left boundary, and the vertical component of the velocity is set to zero over both the upper and lower walls; the right boundary is left free (zero traction is prescribed). A dynamic viscosity coefficient $\mu = 0.01$ and a density $\rho = 1$ are used. These parameters result in a Reynolds number (Re) of 100. The spatial domain is discretized with an unstructured uniformly distributed mesh of nearly 30,000 linear triangular elements, shown in Fig. 7(b).

This case was computed with three different time step sizes and time adaptivity criteria. First, a simulation was conducted using a variable time step size BDF2 scheme with the time-adaptive algorithm based on a fractional step scheme described in Algorithm 1. The initial time step size for the simulation was $\delta t_0 = 0.5$. Note that it is essential to choose an initial time step small enough to ensure that the simulation does not reach a steady state until the time adaptivity algorithm is activated. The time interval for the entire simulation was [0,500]. This first simulation provides the optimized distribution of time steps, δt_{var}, from which it is possible to extract an average time step, δt_{av}, and a minimum time step, δt_{min}, after excluding the initial transient interval [0,100]. Secondly, a simulation was computed using the average, δt_{av}, as the constant time step size of the BDF2 scheme. Thirdly, the computation was repeated with the minimum time step size, δt_{min}, as the constant time step size of the BDF2 scheme.

The comparison of these three computations shows the performance of the proposed time-adaptive algorithm. Eight points around the cylinder were chosen to compute the Fourier Trans-

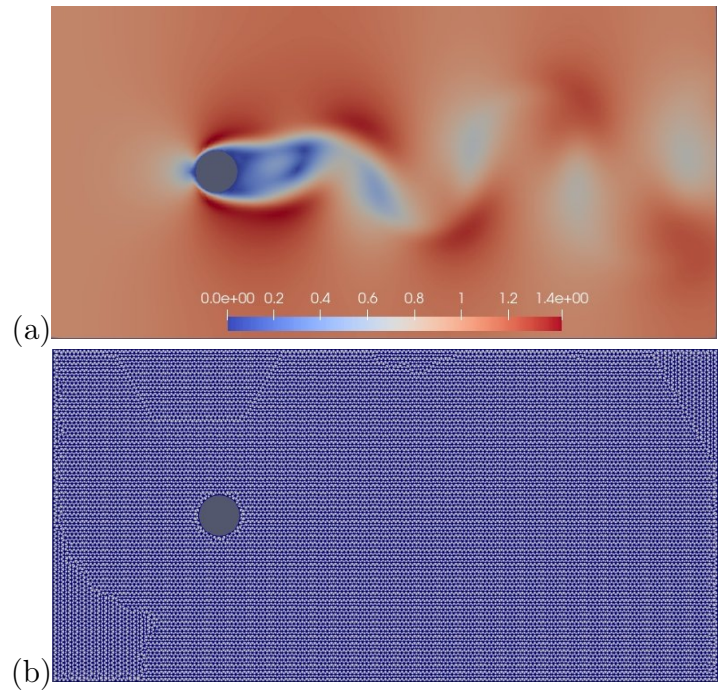

Figure 7: Incompressible viscous flow over cylinder: (a) velocity contour for the case with $\delta t_{\min}$ at $t = 62.0$,(b) mesh configuration for the whole domain

form (FT) of the pressure evolution in time. The objective is to check that the variable time step, δt_{var}, improves the solution obtained with the average time step, δt_{av}, while retaining a similar computational cost. Table 4 presents the details of this study. Since all three simulations share the same frequency, this table only presents the amplitudes of the pressure evolution. The improvement is relative to the solution computed with $\delta t_{\min}$.

Point	Amp $\delta t_{\min}$	Amp δt_{av}	Amp δt_{var}	% improvement
$1(0,-1)$	571.225	220.081	283.935	18.18
$2(0,-2)$	137.725	49.490	65.991	18.70
$3(0,+1)$	574.952	261.722	315.495	17.17
$4(0,+2)$	139.589	69.188	81.360	17.29
$5(-1,0)$	972.185	406.254	504.525	17.36
$6(-2,0)$	488.141	203.570	252.606	17.23
$7(+4,0)$	326.290	137.686	172.084	18.24
$8(+6,0)$	253.441	110.273	139.667	20.53

Table 4: Pressure amplitude of the incompressible flow over the cylinder for the constant BDF2 simulation with the minimum (min) and average (av) time step sizes, as well as with variable (var) time step size, at eight different points. The coordinates of these points are relative to the center of the cylinder.

Table 4 indicates that for an incompressible flow using a fractional step algorithm, the proposed time error indicator shows considerable improvement for all the points compared to the constant BDF2 scheme with average time step size. In the following examples, the performance of the time adaptive algorithm in isentropic cases is discussed.

6.3. Aeolian tones of low Mach isentropic viscous flow

The following benchmark example involves a uniform flow past a 2D cylinder with a diameter (D) of 0.3 units at the center of a square domain with a length of 200 units. The incident velocity on the left boundary is set to $(20, 0)$. The dynamic viscosity coefficient is taken as $\mu = 0.006$ and the density as $\rho = 1$, which results in Reynolds and Mach numbers in the far field of $\mathrm{Re} = 1000$ and $\mathrm{Ma} = 0.0583$, respectively. This scenario helps to evaluate the aeolian tones of radiated sound in a low Mach viscous isentropic flow.

The boundary conditions are prescribed as proposed in [41]. As explained in this reference, a filtering frequency of 50 is used to avoid reflections at the external boundaries, and the velocity prescription of both upper and lower walls is done weakly using $\beta_0 = 10$. Nearly $225,000$ linear triangular elements were used in this simulation, the mesh size near the cylinder walls being $3 \times 10^{-2} D$. The mesh size on the surface around the cylinder is $0.27D$, and in the far field it is $3.33D$. Snapshots of pressure and velocity contours intended to understand the flow and details of the finite element mesh employed are shown in Fig. 8.

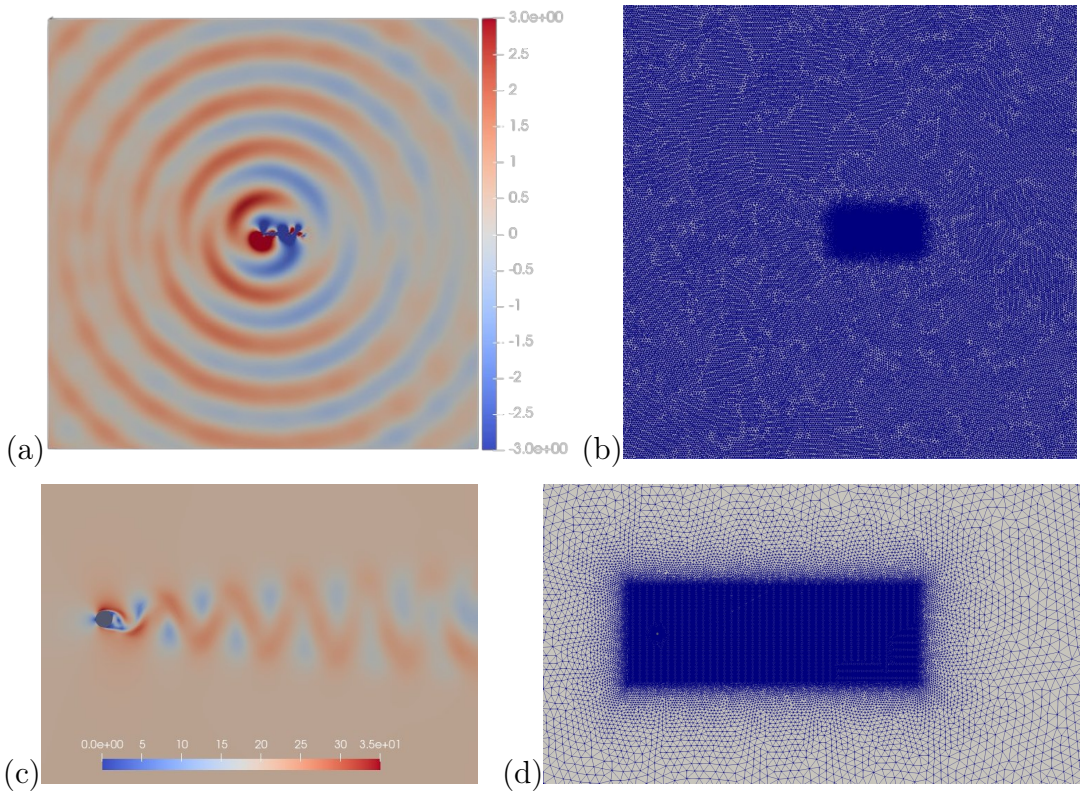

Figure 8: Aeolian tones: (a) Pressure contours using $\delta t_{\min}$ at $t = 0.485$. (b) Finite element mesh for the whole domain. (c) Velocity contours using $\delta t_{\min}$ at $t = 0.485$ in the near field. (d) Close up of the finite element mesh.

As in the incompressible case, three calculations were carried out varying the time step size (δt_{var}, δt_{av} and $\delta t_{\min}$). The initial time step size for the variable time step simulation was taken as $\delta t_0 = 3 \times 10^{-3}$; this small value is needed for accurately reproducing the aeroacoustic signals. In this case, a second-order variable time step size BDF2 scheme was used for the time evolution, and the time interval for the entire simulation was $[0, 9]$. Similarly to the previous numerical example, the minimum, $\delta t_{\min}$, and the average, δt_{av}, time step sizes were established from the time adaptive variable simulation in the $[2, 9]$ time window, and two additional simulations with constant time step sizes were conducted.

Six points around the cylinder were chosen to compute the Fourier transform of the pressure time evolution. The flow displays two dominant frequencies, $\omega_1 \approx 15$ and $\omega_2 \approx 30$. The former corresponds to the large structures, which we call *mechanical*, and the latter to the small amplitudes that propagate much further away and can be identified as the acoustic component of the flow. Table 5 presents the amplitudes obtained in each case for the mechanical and the acoustic pressure components. It is observed that δt_{var} yields a significant improvement of the results compared to those of δt_{av} (relative to those of δt_{min}). This improvement is particularly significant for the acoustic component of the pressure.

Point	Amp δt_{min}		Amp δt_{av}		Amp δt_{var}		% improvement	
	Mechanical	Acoustic	Mechanical	Acoustic	Mechanical	Acoustic	Mechanical	Acoustic
$1(0,-2)$	157.440	3.192	136.14	3.660	140.050	3.083	18.36	76.73
$2(0,-6)$	75.672	1.017	66.120	1.240	66.990	1.090	8.37	67.47
$3(0,+2)$	157.132	4.210	135.883	4.852	140.306	4.570	20.82	44.02
$4(0,+6)$	75.593	2.160	65.795	2.073	66.749	2.190	9.745	66.27
$5(-2,0)$	-	23.640	-	25.999	-	25.713	-	12.12
$6(-6,0)$	-	13.097	-	14.891	-	14.462	-	23.93

Table 5: Pressure amplitudes for the mechanical and acoustic pressure components for the aeolian tones example at different points, with coordinates referred to the center of the cylinder. The amplitude of the mechanical component is negligible at points 5 and 6. The convention is the same as in Table 4.

6.4. Aerodynamic sound radiated by flow past an airfoil

The ensuing example involves uniform flow over a NACA 0012 airfoil with an angle of attack of 5°. This case will serve as an additional qualitative validation of the proposed time error indicator and the associated adaptive strategy. Similarly to the previous example, the vortex shedding phenomenon arises from the pressure pulses emitted by the airfoil's surface. This specific example has been analyzed by [41, 42] to investigate the propagation of acoustic scales and to demonstrate the solver's ability to reproduce flow patterns at a Mach number of 0.4. Additionally, it showcases the implementation's capability to handle 3D configurations while avoiding spurious reflections at the external boundaries. However, the primary goal in this example is to assess the performance of the proposed time error indicator.

The exterior of the computational domain is a cylinder of diameter $R = 10$ and width $W = 1$ in the perpendicular direction; the coordinates in the circular section are denoted (x, y), and z is the coordinate across the width. The airfoil, which has a constant section and extends across the whole width of the domain, has its trailing edge at the center of the cylinder, and its chord line is $d = 0.1524$ units long. For the simulation, the computational domain has been discretized using a semi-structured mesh, consisting of around 7,200,000 linear tetrahedral elements.

For the prescription of the boundary conditions in the x and y directions, a PML has been used, the same as the one that was used in [42], with the only difference that inside the PML the velocity is prescribed to the inlet velocity. Moreover, periodic boundary conditions have been assigned to the walls in the z direction. The incident horizontal velocity on the left surface has been set to $\mathbf{u} = (140, 0, 0)$. The viscosity has been taken as $\mu = 2.56 \times 10^{-3}$ and the density as $\rho = 1.2$. As a result, the Reynolds number is $\text{Re} \approx 10,000$ and the Mach number is $\text{Ma} = 0.4$.

As in previous cases, three calculations were carried out varying the time step size of the BDF2 scheme (δt_{var}, δt_{av} and δt_{min}). The time interval for the entire simulation is $[0, 0.25]$. In the variable time stepping case, the initial time step size for the simulation has been fixed to $\delta t_0 = 4 \times 10^{-5}$

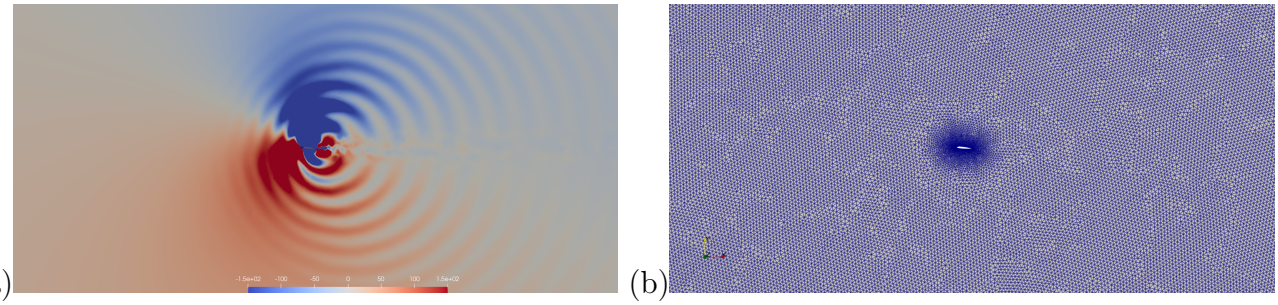

Figure 9: Flow past a NACA 0012 airfoil: (a) close-up view of the pressure field around the airfoil (scaled at $\mp 150Pa$),(b) mesh configuration around the wing.

and the chord length of the wing has been taken to be the characteristic length for this example. Throughout the simulation, the CFL condition was calculated and monitored, remaining within a range of 1 to 15. Similarly, the minimum, δt_{min} and the average, δt_{av}, time step sizes have been established from the time adaptive variable simulation in the $[0.1, 0.25]$ time window, and two additional simulations with constant time step sizes have been conducted.

Fig. 9 shows the pattern of the acoustic pressure waves obtained and the finite element mesh employed around the wing in the cross-section of the domain.

The performance of the time adaptive algorithm for this problem can be further established by the Fourier analysis of the pressure time evolution. Five sets of coordinates (x, y) around the wing have been selected based on the results of the simulation. While various points across the width were analyzed, the z-coordinate does not impact the behavior in the frequency domain due to the periodic boundary conditions. The acoustic frequency, identified as that corresponding to the pressure modes that propagate far from the wing, has been found to be $\omega \approx 1,800$. Table 6 presents the results of the pressure amplitudes obtained for this frequency. It can be seen that the solution obtained using δt_{var} shows a significant improvement compared to the solution obtained with δt_{av}, while the computational cost is of the same order.

Point	Amp δt_{min}	Amp δt_{av}	Amp δt_{var}	% improvement
$1(0,-1)$	0.129	0.131	0.130	54.66
$2(0,-2)$	0.0075	0.0087	0.0076	94.17
$3(0,+1)$	0.1385	0.1414	0.1387	91.39
$4(0,+2)$	0.00714	0.008442	0.007169	97.87
$5(-1,0)$	0.007417	0.008892	0.007455	97.46

Table 6: Pressure amplitudes for the acoustic pressure component for the flow over the wing at different points, with coordinates referred to the trailing edge of the wing. The convention is the same as in Table 4.

7. Conclusions

In this study, an a posteriori time error indicator has been introduced for incompressible and isentropic flows. Initially, variable time step size BDF2 and BDF3 schemes have been presented to leverage the capabilities of the proposed time error indicator. The suggested time error indicator has been applied to the VMS-stabilized finite element flow solver for both the monolithic and fractional step algorithms for isentropic flows reported in [42, 41], respectively. The proposed

approaches have been validated and tested using examples from manufactured solutions and benchmark cases. An adaptive time step refinement strategy has also been developed, utilizing time and spatial error indicators to manage errors associated with time discretization.

In the monolithic scheme, the convergence studies with incompressible and isentropic formulations for the manufactured solutions have shown that the proposed time error indicator has the correct convergence tendency and slightly more error than the actual error in the asymptotic region for all time step sizes. Therefore, users can confidently use the time error indicator for monolithic algorithms without any modifications.

In the case of the fractional step algorithm, an additional term for the time error indicator is suggested to account for the new error source introduced by the segregation technique. The balance in the total error between that coming from the approximation of the time derivative and that coming from the splitting is modeled by a coefficient κ. An expression for this coefficient has been proposed, but it is likely that it needs to be adjusted depending on the type of problem.

In the proposed time adaptivity algorithm, no grid refinement is intentionally done to independently measure the performance and the improvements of the time step size refinement. The algorithm depends on two user defined parameters which have been adjusted with representative simulations. The variable time step size simulations with the time adaptivity algorithm showed remarkable enhancements in accuracy with respect to a constant time step size calculation with the same number of time steps, and therefore with a similar computational effort.

Finally, it is worth noting that, since the time and spatial errors are coupled, using only the proposed time-adaptive algorithm does not take into account spatial errors. To address this issue, a possibility to be explored in the future is to combine the adaptive time step size refinement with an adaptive spatial mesh size refinement.

Acknowledgements

J. Sekhavati gratefully acknowledges the support received from the European Union's Horizon 2020 research and innovation program under the Marie Sklodowska-Curie grant agreement No. 955923. R. Codina gratefully acknowledges the support received from the ICREA Acadèmia Program, from the Catalan Government. I. Martínez-Suárez gratefully acknowledges the support received from the Agència de Gestió d'Ajuts i de Recerca (AGAUR) through the predoctoral FI grant 2022-FI-B-00517.

References

[1] G. Akrivis and P. Chatzipantelidis. A posteriori error estimates for the two-step backward differentiation formula method for parabolic equations. *SIAM Journal on Numerical Analysis*, 48(1):109–132, Jan. 2010.

[2] I. Babuška. Error-bounds for finite element method. *Numerische Mathematik*, 16(4):322–333, Jan. 1971.

[3] S. Badia and R. Codina. Algebraic pressure segregation methods for the incompressible Navier-Stokes equations. *Archives of Computational Methods in Engineering*, 15(3):343–369, May 2008.

[4] J. Baiges and R. Codina. Variational Multiscale error estimators for solid mechanics adaptive simulations: An Orthogonal Subgrid Scale approach. *Computer Methods in Applied Mechanics and Engineering*, 325:37–55, 2017.

[5] S. Balay, S. Abhyankar, M. F. Adams, J. Brown, P. Brune, K. Buschelman, L. Dalcin, V. Eijkhout, W. D. Gropp, D. Kaushik, M. G. Knepley, D. A. May, L. C. McInnes, R. T. Mills, T. Munson, K. Rupp, P. Sanan, B. F. Smith, S. Zampini, H. Zhang, and H. Zhang. Petsc web page. `http://www.mcs.anl.gov/petsc`, 2015. [Accessed 25-09-2024].

[6] F. Basile, J.-B. Chapelier, M. de la Llave Plata, R. Laraufie, and P. Frey. Unstructured h- and hp-adaptive strategies for discontinuous Galerkin methods based on a posteriori error estimation for compressible flows. *Computers & Fluids*, 233:105245, Jan. 2022.

[7] J.-P. Berenger. A perfectly matched layer for the absorption of electromagnetic waves. *Journal of computational physics*, 114(2):185–200, 1994.

[8] C. Bernardi and R. Verfürth. A posteriori error analysis of the fully discretized time-dependent Stokes equations. *ESAIM: Mathematical Modelling and Numerical Analysis*, 38(3):437–455, May 2004.

[9] S. Berrone and M. Marro. Space–time adaptive simulations for unsteady Navier-Stokes problems. *Computers & Fluids*, 38(6):1132–1144, June 2009.

[10] S. Berrone and M. Marro. Numerical investigation of effectivity indices of space-time error indicators for Navier–Stokes equations. *Computer Methods in Applied Mechanics and Engineering*, 199(25–28):1764–1782, May 2010.

[11] A. Boisneault, S. Dubuis, and M. Picasso. An adaptive space-time algorithm for the incompressible Navier-Stokes equations. *Journal of Computational Physics*, 493:112457, Nov. 2023.

[12] Y. Bourgault, M. Picasso, F. Alauzet, and A. Loseille. On the use of anisotropic a posteriori error estimators for the adaptative solution of 3D inviscid compressible flows. *International Journal for Numerical Methods in Fluids*, 59(1):47–74, Apr. 2008.

[13] F. Brezzi. On the existence, uniqueness, and approximation of saddle-point problems arising from Lagrange multipliers. *RAIRO - Analyse Numérique*, 8(2):129–151, 1974. Available online at NUMDAM.

[14] J. Cao. Application of a posteriori error estimation to finite element simulation of compressible Navier-Stokes flow. *Computers & Fluids*, 34(8):991–1024, Sept. 2005.

[15] M. Carpenter, S. Viken, and E. Nielsen. The temporal efficiency of higher order schemes. In *41st Aerospace Sciences Meeting and Exhibit*. American Institute of Aeronautics and Astronautics, Jan. 2003.

[16] A. J. Chorin. Numerical solution of the Navier-Stokes equations. *Mathematics of Computation*, 22(104):745–762, 1968.

[17] A. J. Chorin. On the convergence of discrete approximations to the Navier-Stokes equations. *Mathematics of Computation*, 23(106):341–353, 1969.

[18] R. Codina. Stabilized finite element approximation of transient incompressible flows using orthogonal subscales. *Computer Methods in Applied Mechanics and Engineering*, 191:4295–4321, 2002.

[19] R. Codina. On *hp* convergence of stabilized finite element approximations of the convection-diffusion equation. *SeMA Journal*, 75:591–606, 2018.

[20] R. Codina, S. Badia, J. Baiges, and J. Principe. Variational Multiscale Methods in Computational Fluid Dynamics. *Encyclopedia of Computational Mechanics Second Edition*, page 1–28, 2017.

[21] R. Codina, R. Reyes, and J. Baiges. A posteriori error estimates in a finite element VMS-based reduced order model for the incompressible Navier-Stokes equations. *Mechanics Research Communications*, 112:103599, 2021.

[22] R. Codina and O. C. Zienkiewicz. CBS versus GLS stabilization of the incompressible Navier-Stokes equations and the role of the time step as stabilization parameter. *Communications in Numerical Methods in Engineering*, 18:99–112, 2002.

[23] T. Colonius and S. K. Lele. Computational aeroacoustics: progress on nonlinear problems of sound generation. *Progress in Aerospace Sciences*, 40(6):345–416, Aug. 2004.

[24] F. El Chami and T. Sayah. A posteriori error estimators for the fully discrete time dependent Stokes problem with some different boundary conditions. *Calcolo*, 47(3):169–192, June 2010.

[25] O. El Moutea, N. Nakbi, A. El Akkad, A. Elkhalfi, L. El Ouadefli, S. Vlase, and M. L. Scutaru. A mixed finite element approximation for time-dependent Navier–Stokes equations with a general boundary condition. *Symmetry*, 15(11):2031, Nov. 2023.

[26] M. Emmett, E. Motheau, W. Zhang, M. Minion, and J. B. Bell. A fourth-order adaptive mesh refinement algorithm for the multicomponent, reacting compressible Navier-Stokes equations. *Combustion Theory and Modelling*, 23(4):592–625, Jan. 2019.

[27] F. Fambri, M. Dumbser, and O. Zanotti. Space–time adaptive ADER-DG schemes for dissipative flows: Compressible Navier-Stokes and resistive MHD equations. *Computer Physics Communications*, 220:297–318, Nov. 2017.

[28] K. J. Fidkowski and Y. Luo. Output-based space–time mesh adaptation for the compressible Navier-Stokes equations. *Journal of Computational Physics*, 230(14):5753–5773, June 2011.

[29] K.-Y. Fung and H. Ju. Time-domain impedance boundary conditions for computational acoustics and aeroacoustics. *International Journal of Computational Fluid Dynamics*, 18(6):503–511, Aug. 2004.

[30] B. García-Archilla and J. Novo. Robust error bounds for the Navier-Stokes equations using implicit-explicit second-order BDF method with variable steps. *IMA Journal of Numerical Analysis*, 43(5):2892–2933, Oct. 2022.

[31] C. J. Greenshields and J. M. Reese. Rarefied hypersonic flow simulations using the Navier-Stokes equations with non-equilibrium boundary conditions. *Progress in Aerospace Sciences*, 52:80–87, July 2012.

[32] G. Hauke, D. Fuster, and F. Lizarraga. Variational multiscale a posteriori error estimation for systems: The Euler and Navier-Stokes equations. *Computer Methods in Applied Mechanics and Engineering*, 283:1493–1524, 2015.

[33] P. Houston, R. Rannacher, and E. Süli. A posteriori error analysis for stabilised finite element approximations of transport problems. *Computer Methods in Applied Mechanics and Engineering*, 190:1483–1508, 2000.

[34] T. Hughes, G. Feijóo, L. Mazzei, and J. Quincy. The variational multiscale method–a paradigm for computational mechanics. *Computer Methods in Applied Mechanics and Engineering*, 166:3–24, 1998.

[35] T. J. R. Hughes, G. Scovazzi, and L. P. Franca. Multiscale and stabilized methods. *Encyclopedia of Computational Mechanics Second Edition*, page 1–64, Nov. 2017.

[36] M. A. Khanwale, K. Saurabh, M. Fernando, V. M. Calo, H. Sundar, J. A. Rossmanith, and B. Ganapathysubramanian. A fully-coupled framework for solving Cahn-Hilliard Navier-Stokes equations: Second-order, energy-stable numerical methods on adaptive octree based meshes. *Computer Physics Communications*, 280:108501, Nov. 2022.

[37] O. A. Ladyzhenskaya, R. A. Silverman, J. T. Schwartz, and J. E. Romain. The mathematical theory of viscous incompressible flow. *Physics Today*, 17(2):57–58, Feb. 1964.

[38] Z. Li and H.-l. Liao. Stability of variable-step BDF2 and BDF3 methods. *SIAM Journal on Numerical Analysis*, 60(4):2253–2272, Aug. 2022.

[39] J. A. A. Manco and M. T. de Mendonca. Comparative study of different non-reflecting boundary conditions for compressible flows. *Journal of the Brazilian Society of Mechanical Sciences and Engineering*, 41(10), Sept. 2019.

[40] P. H. Oosthuizen and W. E. Carscallen. *Introduction to compressible fluid flow*. CRC press, 2013.

[41] S. Parada, J. Baiges, and R. Codina. A fractional step method for computational aeroacoustics using weak imposition of Dirichlet boundary conditions. *Computers & Fluids*, 197:104374, Jan. 2020.

[42] A. Pont, R. Codina, J. Baiges, and O. Guasch. Unified solver for fluid dynamics and aeroacoustics in isentropic gas flows. *Journal of Computational Physics*, 363:11–29, June 2018.

[43] H. Takemoto, P. Mokhtari, and T. Kitamura. Acoustic analysis of the vocal tract during vowel production by finite-difference time-domain method. *The Journal of the Acoustical Society of America*, 128(6):3724–3738, Dec. 2010.

[44] R. Témam. Sur l'approximation de la solution des équations de Navier-Stokes par la méthode des pas fractionnaires (i). *Archive for Rational Mechanics and Analysis*, 32(2):135–153, Jan. 1969.

[45] H. A. van der Vorst. Bi-CGSTAB: A fast and smoothly converging variant of Bi-CG for the solution of nonsymmetric linear systems. *SIAM Journal on Scientific and Statistical Computing*, 13(2):631–644, Mar. 1992.

[46] R. Verfürth. A posteriori error analysis of space-time finite element discretizations of the time-dependent Stokes equations. *Calcolo*, 47(3):149–167, Jan. 2010.

[47] R. Verfürth. *A posteriori error estimation techniques for finite element methods*. Oxford University Press, 2013.

[48] G. Wanner and E. Hairer. *Solving Ordinary Differential Equations II*, volume 375. Springer Berlin Heidelberg New York, 1996.

[49] O. C. Zienkiewicz and J. Z. Zhu. The superconvergent patch recovery and a posteriori error estimates. Part 1: The recovery technique. *International Journal for Numerical Methods in Engineering*, 33(7):1331–1364, May 1992.

[50] O. C. Zienkiewicz and J. Z. Zhu. The superconvergent patch recovery and a posteriori error estimates. Part 2: Error estimates and adaptivity. *International Journal for Numerical Methods in Engineering*, 33(7):1365–1382, May 1992.